Winter 12-15-2023

OPTIMIZATION OF TRANSITION-METAL INCLUSIVE CARBON AEROGELS FOR ELECTROCHEMICAL ENERGY APPLICATIONS

Allen Dalton Davis
Pittsburg State University, allen.davis@gus.pittstate.edu

OPTIMIZATION OF TRANSITION-METAL INCLUSIVE CARBON AEROGELS FOR ELECTROCHEMICAL ENERGY APPLICATIONS

A Thesis Submitted to the Graduate School
in Partial Fulfillment of the Requirements
For the Degree of
Master of Science

Allen Dalton Davis

Pittsburg State University

Pittsburg, Kansas

December 2023

OPTIMIZATION OF TRANSITION-METAL INCLUSIVE CARBON AEROGELS FOR ELECTROCHEMICAL ENERGY APPLICATIONS

Allen Dalton Davis

APPROVED:

Thesis Advisor _____
Dr. Ram Gupta, Department of Chemistry

Committee Member _____
Dr. Charles Neef, Department of Chemistry

Committee Member _____
Dr. Khamis Siam, Department of Chemistry

Committee Member _____
Dr. Timothy Dawsey, National Institute for Materials Advancement

Acknowledgements

I am immensely grateful for the support and guidance I have received throughout this academic journey, and I would like to express my deepest appreciation to the individuals who have played important roles in my success.

First and foremost, I extend my heartfelt gratitude to my thesis advisor and mentor Dr. Ram Gupta. Your mentorship has been invaluable, and your unwavering support has allowed me to surmount this peak of my academic journey. Your expertise, patience, and dedication to my intellectual growth have left a noteworthy mark on my academic understanding.

I am also grateful to my esteemed thesis committee and the additional professors whose insights and feedback have been and will be instrumental in shaping the quality of my work. To Dr. Siam and Dr. Dawsey, I am most grateful for the individual tips and guidance for constructing this document and presentation. To Dr. Neef, for your guidance in organic chemistry and encouragement for me to deeper develop my critical thinking skills. To the innumerable professors at Pittsburg State University who have helped me on this journey, I also give thanks. Surely, each of you demonstrated a certain commitment to excellence which alongside your willingness to share knowledge has significantly enriched my academic understanding.

To my coworkers and colleagues at NIMA, your camaraderie and collaborative spirit have made this academic journey all the more enjoyable. The shared moments of discussing presentation structure and working out problems have been integral to the

development of my ideas, and I appreciate the sense of community we have fostered together.

To my family, your unconditional love and unwavering belief in my abilities have been a constant source of strength. To my mom I am thankful for the many lunches we shared, giving me brief respite from my college-budget diet, and allowing me to clear my mind. To my dad, the unrelenting push towards excellence has gotten me to where I am today. Furthermore, I extend gratitude to my extended family, whose well wishes, and many visits further spurred my success. Surely, each of your sacrifices and encouragement have provided the cornerstone of my achievements, and I am forever grateful for the foundation of support you have provided.

Last but certainly not least, to my fiancé Sarah, your love and understanding have been my anchor throughout this journey. Your patience during late nights and your encouragement during moments of self-doubt have been the pillars that held me up. I am profoundly thankful for your presence in my life.

Altogether, his journey would not have been possible without the collective support of these remarkable individuals. Each of you has played a unique and vital role in my academic and personal growth, and I am truly blessed to have such an incredible network of mentors, colleagues, and loved ones. As I move forward, I carry with me the lessons learned and the relationships forged during this chapter of my life, and I am excited to continue my journey with the wisdom and support you have provided. Thank you from the depths of my heart and the peak of my mind.

OPTIMIZATION OF TRANSITION-METAL INCLUSIVE CARBON AEROGELS FOR ELECTROCHEMICAL ENERGY APPLICATIONS

An Abstract of the Thesis by
Allen Dalton Davis

The ever-growing need for energy alongside rising concerns for climate change demands the development of renewable energy technologies. Hydrogen fuel cells are a promising technology that can serve to either supplement energy generation or act as a lone power source. Yet for these devices to be truly green, the hydrogen that serves as fuel must be procured from a renewable resource. Electrolytic water splitting is a process that allows for the dissociation of water into H_2 and O_2. For this process to be practical, the electrolyzer needs to demonstrate high efficiency and stability, as well as a low overhead cost. Towards this end, transition-metal-based electrocatalysts demonstrate the desired properties.

In this study, transition-metal inclusive carbon aerogels (RF-CT_m) were initially synthesized by adding nickel acetate (RF-CNi), cobalt acetate (RF-CCo), or a 1:1 weight ratio of both (RF-CCoNi) to a resorcinol-formaldehyde (RF) hydrogel synthesis. The resulting hydrogels were then lyophilized to create their respective aerogels, followed by a calcination process to carbonize them. After synthesis, the various samples were employed towards electrode construction for use as bifunctional electrocatalysts. Furthermore, the initial success of RF-CCoNi encouraged the creation of more samples, which modified the wt.% of the 1:1 metal mixture added to the hydrogel synthesis.

Initial electrochemical testing demonstrated that the materials possessed a high affinity for the oxygen evolution reaction, with RF-C, RF-CCo, RF-CNi, and RF-CCoNi producing low overpotentials of 320, 360, 330, and 310 mV respectively. Additionally,

these materials processed the reaction at a high rate, with corresponding Tafel slopes being 79, 65, 65, and 47 mV/dec. Meanwhile, the material provided solid results for the hydrogen evolution reaction, demonstrating overpotentials of 236, 207, 202, and 141 mV alongside Tafel slopes of 203, 168, 142, and 131 mV/dec. Considering the promising results of RF-CCoNi, further testing explored the adjustment of overall metal content added to the aerogel. The resulting samples, delineated as RF-CCoNi 25%, RF-CCoNi 50%, RF-CCoNi 75%, and RF-CCoNi 150% demonstrated oxygen evolution and hydrogen evolution overpotentials of 310, 370, 360, 360, and 188, 134, 158, 340 mV each. The results from these experiments advocate that RF-CCoNi aerogels possess desirable properties as a bifunctional electrocatalyst for water electrolysis.

TABLE OF CONTENTS

LIST OF TABLES

LIST OF FIGURES

CHAPTER I

INTRODUCTION

1.1 The importance of energy

According to Nobel laureate Dr. Richard Smalley, energy is the largest issue humanity will need to overcome in the near future [1]. This prediction, made around the turn of the century, has thus far proven accurate. Energy and/or its storage is mentioned daily in the news, with modern infrastructure being reliant on consistent energy generation. Yet energy production is only a facet of the issue when sustainability and climate change are considered. Growing awareness of the limitations inherent to fossil fuels has created a massive drive towards renewable green energy solutions. These limitations include the generation of greenhouse gas emissions, the overhanging threat of resource scarcity, and a lack of diversity in petrochemical products. In terms of greenhouse gas emissions, fossil fuels are responsible for the majority of CO_2 released into the atmosphere [2]. Other common greenhouse gases that are involved with fossil fuel usage include nitrous oxides (NO_2), methane (CH_4), and water vapor (H_2O). These emissions variably lead to global warming and/or ocean acidification, which in turn causes harm to the global ecosystem. Meanwhile, the finite amounts of oil available on the earth means that the total supply will eventually run out. Due to society's massive reliance on petroleum, many of the most easily available deposits have already been exploited. Subsequently, a large percentage of

the remaining deposits require vast amounts of time, manpower, and machinery to extract from reserves deep in the earth. As the oil well drains, the energy required to extract drilled oil outweighs its cost. Eventually, this fate will befall all known oil wells, leading to an international shortage. While this problem may seem distant, recent conflicts have demonstrated the need for sustainable energy access [3]. Finally, while gasoline, coal, and natural gas are popular choices for energy generation, they are derived from a handful of sources, often with harsh methods of extraction. This issue is most notable when economic scarcity is considered. Given that most of America's infrastructure is reliant on petroleum or natural gas, a shortage of one or the other equates to higher energy prices. While these problems plague the current energy infrastructure, many solutions are being implemented and explored. One option is to reduce, then completely replace fossil fuels with renewable energy sources. As opposed to petrochemical energy, renewable energy relies on naturally occurring phenomena to transform different forms of energy into electricity. Examples of these sources include solar, wind, hydroelectric, and geothermal power. Regardless of the specific source, renewable energy offers sustainable alternative fuel sources that directly counter many of the issues seen in fossil fuels.

1.2 Importance of energy storage

While renewable energy addresses the problems of sustainability, these resources in turn face a few issues. First, renewable energy is environmentally dependent. To be cost-effective, wind turbines and solar panels require areas with wide access to wind and sunlight respectively. Just as well, hydroelectric and geothermal power require the presence of specific geological features to even be considered for use. These issues

coincide with inconsistent energy generation, which is especially pertinent among solar and wind. While petrol plants can adjust the amount of fuel burned in line with energy demands, many green energy sources are at the mercy of nature. Meanwhile, regardless of the power source used, more energy is generated than required to prevent blackouts, leading to wastage. Thankfully, a simple solution to these problems is to invest in energy storage. Supplemental energy storage is already standard practice in the modern energy grid [4]. When demand is low, excess power is allocated to the energy storage medium of choice. Then, when demand spikes, energy is extracted to supplement power needs. This process allows for stability in an otherwise volatile industry. While there are many options available for supplemental energy storage, hydrogen fuel cells are among the most attractive. In general, fuel cells are energy-generating devices that converts chemical energy into electric current. The attractiveness of hydrogen fuel cells is due to their high efficiency, green byproducts, and negligible emissions. Like batteries, fuel cells rely on electrochemical redox reactions to generate electricity. Unlike batteries, fuel cells require a constant application of fresh reactants to fuel the reaction. In the case of hydrogen fuel cells, these reactants are diatomic hydrogen and oxygen. While oxygen is abundantly available, dihydrogen is a much more limited resource. Industrially, most H_2 is generated via steam methane reforming and coal gasification [5]. These are violent, high pressure and high temperature, processes that transform their respective fuel sources into hydrogen, carbon monoxide, and carbon dioxide. While this process is certainly effective, it faces the same issues seen with other fossil fuels, making its use in sustainable energy questionable. Further considerations for a cyclic hydrogen economy include hydrogen storage, transportation, and of course, safety concerns. When compared to fuel like oil, gas, and

methane, hydrogen is somewhat difficult to store. This is due to hydrogen's low volumetric energy density and minute molecular size. To counter these limitations, many solutions have been developed and explored. The most common solutions include gas compression, hydrogen liquification and chemical storage. Gas compression is a simple solution to the problem, that involves storing hydrogen gas within a high-pressure tank. These tanks can either be completely hollow or filled with porous, high surface area materials to further enhance storage capacity. Hollow tanks are inexpensive but suffer from low energy density. Meanwhile, filled tanks can store more hydrogen per volume via the physisorption effect, but are more expensive [6][7]. Hydrogen liquefaction has the highest energy density per volume, making it a popular option for transportation. However, hydrogen only enters its liquid state at -253 °C at standard pressure, thus it must be kept at extremely low temperatures to be viable. Finally, hydrogen can be stored chemically, with metal hydrides being an extremely popular option for this task [8]. Regrettably, the chemical storage of hydrogen again faces the issues of limited storage capacity and complex equipment requirements. In terms of safety, hydrogen is treated similarly to natural gas given their high flammability, yet extra care must be taken with hydrogen given its propensity to leak and near invisible flame [9]. Altogether, these many concerns and issues initially make hydrogen seem counterproductive to energy storage. However, one final consideration makes this chemical among the most widely researched options for energy conversion and storage, water electrolysis.

1.3 Introduction to water electrolysis

Water electrolysis, also known as electrolytic water splitting, is the process of electrically separating H_2O into its constituent atoms. This reaction can occur when two electrodes are submerged in an aqueous system, whereafter a voltage can be applied to evolve hydrogen at the cathode and oxygen at the anode, as shown below in **Figure 1.1**. Given that pure water is a poor conductor of electricity, an electrolyte is added to the reaction mixture to enhance the reaction kinetics. This is especially noticeable when the electrolyte is acidic or basic, as the pH of the system determines the half-reaction pathways for water splitting. In an acidic system, water is oxidized at the anode, producing O_2 and a handful of protons, which are concurrently reduced into H_2 at the anode. In a basic system, water is instead reduced into H_2 and some hydroxide ions, with said ions oxidizing into O_2 and H_2O. Regardless of the path taken, the result involves splitting two molecules of water to create two H_2 molecules and one O_2 molecule, demonstrated in the following set of equations [5].

Acidic solution

(1) Cathode $$4H^+ + 4e^- \rightarrow 2H_2$$

(2) Anode $$2H_2O \rightarrow 4H^+ + 4e^- + O_2$$

In neutral or basic solution

(1) Cathode $$4H_2O + 4e^- \rightarrow 2H_2 + 4OH^-$$

(2) Anode $$4OH^- \rightarrow 2H_2O + 4e^- + O_2$$

Complete reaction $$2H_2O \rightarrow 2H_2 + O_2$$

While the total process sounds simple on paper, there are many parameters that affect the efficiency of the reaction. Natively, the electrolysis reaction requires a minimum potential difference of 1.23 V at STP [5]. However, due to thermodynamic limitations, the true voltage required is often a fair bit higher. The difference between these two values is the system's overpotential. The efficiency lost due to overpotential can be attributed to many different causes. These limitations range from the activation energy required to jumpstart the reaction to the formation of bubbles that stick to the electrode and limit active site availability. While solutions to correct many of these issues are limited, one prominent solution is to develop effective electrocatalysts.

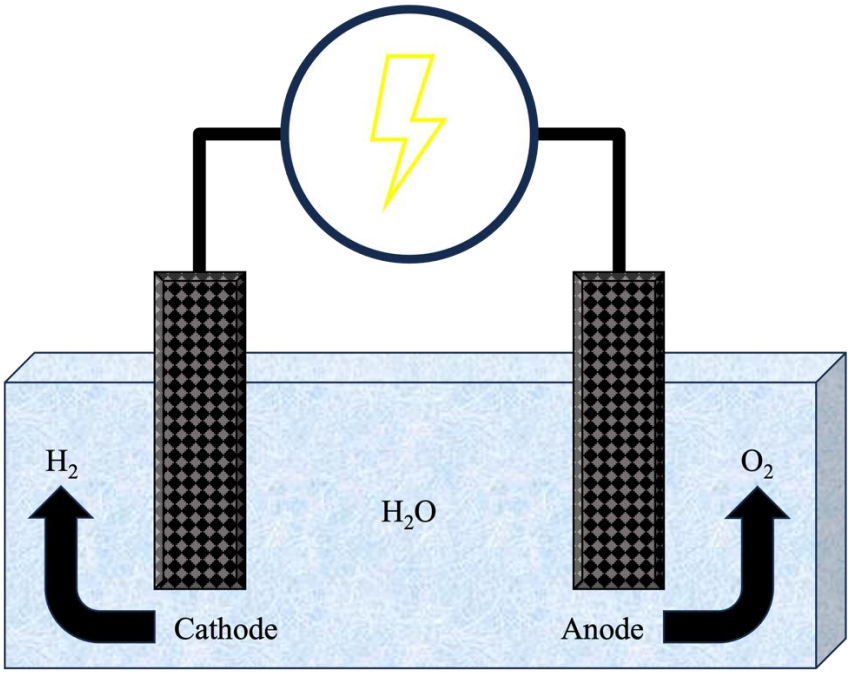

Figure 1.1- Graphic demonstrating a simplified electrolyzer setup.

1.4 Importance of efficient electrocatalysts

Large volumes of research have gone into designing electrocatalysts that efficiently evolve both O_2 and H_2. As of now, the most effective materials observed for reducing overpotential are noble metals and their derivatives. Platinum (HER), iridium oxide (OER), and ruthenium oxide (OER) provide the lowest overpotentials seen for the overall reaction [10]. However, these materials suffer from cost efficiency due to their high cost and low corrosion stability. With this fact in mind, noble metal substitutes have been explored to lower the overhead cost and increase stability. These materials range from various metal sulfides, phosphides, oxides, and hydroxides, to more advanced materials such as metal-organic frameworks, conducting polymers, and graphene-based materials. Each of these materials seeks to improve electrocatalytic properties in their own ways. Metal sulfides, for example, adopt different morphological configurations depending on the set of base metals used. Layered metal sulfides can be readily made into nanosheets, exhibiting enhanced properties at the edges. Meanwhile, non-layered metal sulfides provide a distinct crystalline morphology and exhibit major property differences based on the specific element used [11]. For this study, transition-metal nanoparticles were selected as the electrocatalytically active material, with a resorcinol-based carbon aerogel acting as a substrate to improve electrochemical activity. The rationale for selecting these materials is further explored in **Chapter II**.

1.5 Research objectives

Transition-metal-based electrocatalysts are among the most promising options for water electrolysis. This is due to their high conductivities, available active sites, good chemical stability, and versatile morphologies. Nevertheless, transition metals require extensive modifications to achieve optimal properties for electrocatalysis. Considering this, the purpose of this study was to improve the properties of such materials via their inclusion within the synthesis of carbon aerogels. This was achieved by adding transition-metal acetates to a resorcinol-formaldehyde (RF) hydrogel synthesis. The resulting products were then subjected to further treatment to create transition-metal inclusive carbon aerogels. Portions of the developed carbon aerogels were made into electrodes for electrochemical testing, while the remainder of the samples were preserved for structural analysis.

CHAPTER II

EXPERIMENTAL DETAILS

2.1 Materials

Nickel (II) acetate $\{Ni(CH_3CO_2)_2\}$ tetrahydrate, cobalt (II) acetate $\{Co(CH_3CO_2)_2\}$ tetrahydrate, resorcinol, sodium carbonate, and 37 wt.% formaldehyde were purchased from Fisher Scientific, USA. Meanwhile, polyvinylidene fluoride (PVDF), N-methyl-2-pyrrolidone (NMP), carbon black, and KOH pellets were purchased from MTI Corporation, USA.

2.1.1 Transition-Metals

Transition metals and their derivatives have grown into increasingly popular options as a material for electrocatalyst application. As opposed to noble metals, transition metals are widely abundant and of low cost. As such, while their electrochemical properties are generally lesser, their ease of attainment makes them much more cost-effective. It should be stated that only a limited selection of these metals is amenable to these applications. The limitations associated with some transition metals include toxicity, low electrocatalytic activity, high scarcity, and poor stability. Thankfully, a majority of first row transition metals provide beneficial properties for this use, with Mn, Fe, Co, Ni,

and Cu being particularly popular. These materials often demonstrate beneficial properties, such as high stability, available active sites, and lower cost. Multiple studies have demonstrated the efficacy of transition-metal-based materials in electrochemical applications. Furthermore, additional studies have shown the benefits of using multi-metallic compounds for electrochemistry. For example, Kim et al. synthesized nickel oxide and iron-nickel oxide nanoparticles that demonstrated promising results towards oxygen evolution [12]. These particles were created through hydrothermal synthesis, wherein their morphology was modified by adjusting the synthesis route. In testing, the nickel oxide nanoparticles with both hexagonal and toroid morphology demonstrated overpotentials of 420 mV, while the octahedral nanoparticles provided an overpotential of 450 mV. Meanwhile, the inclusion of iron oxide lowered the overpotentials for all the samples. The hexagonal, toroid, and octahedral iron-nickel oxide nanoparticles had overpotentials of 380 mV, 370 mV, and 380 mV at 10 mA/cm^2 each. This study demonstrates the importance of both nanoparticle size and shape for electrochemical applications, as well as the benefits of using bimetallic compounds.

2.1.2 Carbon Aerogels

Aerogels are a unique class of material that demonstrates high porosity, low density, and extremely low weight. Due to the notable porosity of aerogels, they have a high surface area to match. This fact makes certain varieties of aerogels extremely promising for electrochemical applications. This is because one of the great limitations observed in electrocatalyst application is the available surface area for reactions. Carbon and graphene aerogels are among the most popular options for use in both water splitting

and supercapacitors. Carbon aerogels are unique amongst other types of aerogels because they cannot be directly synthesized. To create a carbon aerogel, a precursor aerogel must first be obtained. These precursor aerogels can be made from a variety of either polymer or bio-based aerogels. Popular options for polymer aerogel precursors include RF aerogels, crosslinked polyimides, and many others [13][14][15][16]. Meanwhile, bio-based aerogels can be made from cellulose, chitosan, and bacteria-derived materials [17][18][19][20]. Graphene aerogels are within the family of carbon aerogels, their notable differences are general increases in the desired properties, albeit at an inflated cost. Graphene aerogels, as their name suggests, are composed entirely of graphene. These aerogels are predominantly made from reduced graphene oxide aerogels, which in turn are created via the hydrothermal synthesis method, followed by calcination [21]. Graphene demonstrates a plethora of properties that translate into their application towards aerogels. These properties include high conductivity, massive surface area, and improved mechanical properties [22]. Despite these advantageous properties, producing graphene is a harsh and expensive undertaking, limiting its general applicability. As such, non-graphene carbon aerogels demonstrate promise as a more cost-effective option. RF aerogels are an extremely popular option for carbon aerogel synthesis due to the low cost of its constituents and facile reaction method. In literature, RF-carbon aerogels have shown potential for wearable sensors, supercapacitors, metal-air batteries, and in this study water splitting applications [23][14][24]. An example of the RF aerogel synthesized in this report, and its subsequent carbon aerogel, can be seen in **Figure 2.1**.

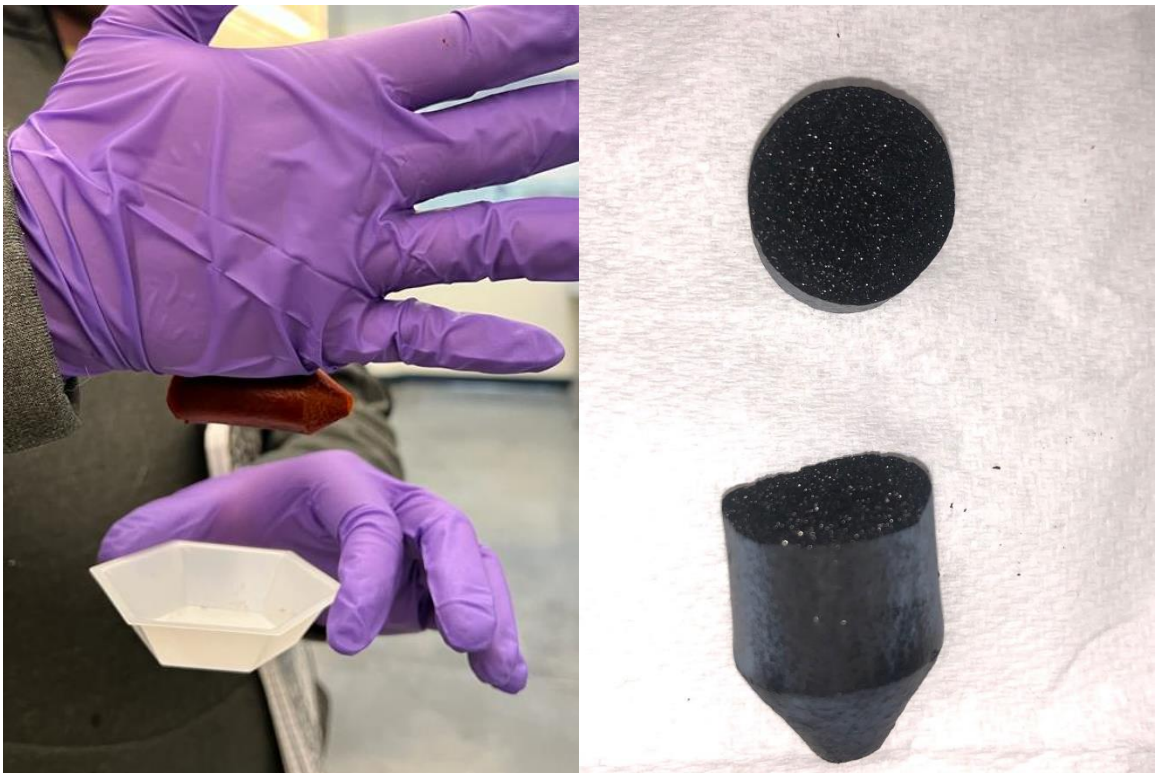

Figure 2.1- RF aerogel held up by static, and subsequent RF-C with cross section.

2.2 Synthesis of metal inclusive carbon aerogels.

2.2.1 Synthesis of RF-C, RF-CCo, and RF-CNi, & RF-CCoNi

The general synthesis scheme for the carbon aerogels occurred over three distinct steps, hydrogel synthesis, lyophilization, and calcination. For the initial hydrogel synthesis, resorcinol (1.00 g) was dissolved in H_2O (47 mL). After total dissolution, 37 wt.% formaldehyde solution (1.8 mL) and Na_2CO_3 catalyst solution (2.4 mL) were added, then the solution was covered and left to stir for 24 h. For RF-CCo, RF-CNi, and RF-CCoNi, 249 mg of their respective metal acetates (124.5 mg of each metal acetate for RF-CCoNi) were then added. After stirring was complete, the samples were evenly divided into two centrifuge tubes per sample and allowed to cure in an oven at 80 °C for 48 h. The

resulting hydrogels were then allowed to cool to room temperature, then frozen for 24 hours in a -20 °C freezer. The frozen samples were then lyophilized in a FreeZone 2.5 L freeze dryer at -80 °C for 72 h. The RF aerogels were finally subjected to calcination under a nitrogen atmosphere in an OTF-1200X tube furnace at 800 °C for 2 hr with a heating rate of 5 °C/min. The final products were then set aside for characterization and testing.

2.2.2 Synthesis of various RF-CCoNis

After testing the initial samples, further investigation of RF-CCoNi was warranted. As such, multiple samples were synthesized that varied the overall metal concentration. These samples were labeled based on their metal wt.% difference from the original RF-CCoNi sample, shown below in **Table 2.1**. These materials were made using the same methods as prior and were also treated for characterization and testing. Examples of RF-CCoNi 10%-40% post lyophilization are shown below in **Figure 2.2**.

Table 2.1- Formulations for different aerogel syntheses.

Sample ID	Resorcinol (g)	Formaldehyde (ml)	Na_2CO_3 Catalyst (ml)	$\{Co(CH_3CO_2)_2\}$ (mg)	$\{Ni(CH_3CO_2)_2\}$ (mg)
RF-C	1.00	1.8	2.4	0	0
RF-CCo	1.00	1.8	2.4	249	0
RF-CNi	1.00	1.8	2.4	0	249
RF-CCoNi	1.00	1.8	2.4	124.5	124.5
RF-CCoNi 25%	1.00	1.8	2.4	31.13	31.13
RF-CCoNi 50%	1.00	1.8	2.4	62.25	62.25
RF-CCoNi 75%	1.00	1.8	2.4	93.38	93.38
RF-CCoNi 150%	1.00	1.8	2.4	186.75	186.75
RF-CCoNi 10%	1.00	1.8	2.4	12.45	12.45
RF-CCoNi 20%	1.00	1.8	2.4	24.9	24.9
RF-CCoNi 30%	1.00	1.8	2.4	37.35	37.35
RF-CCoNi 40%	1.00	1.8	2.4	49.8	49.8

Figure 2.2- RF-CCoNi 10%-40%.

2.3 Structural characterization

Morphological and chemical analysis of the metal inclusive carbon aerogels were collected via X-ray diffraction (XRD), scanning electron microscopy (SEM), and energy-dispersive X-ray analysis (EDS).

2.3.1 XRD

XRD is an analytical technique that is used to observe the different crystalline domains present in a specific material. The XRD apparatus itself is composed of three separate parts, the X-ray tube, sample platform, and X-ray detector. During operation, the X-ray tube shines on the sample while rotating around the platform. Meanwhile, the X-rays scattered from the sample are observed by the detector, which measures the change in intensity of the reflected X-rays at different angles. The data collected from this process was analyzed via Bragg's law ($n\lambda = 2d\sin\theta$), where d is the inter-layer spacing, θ is the diffraction angle, n is the diffraction order, and λ is the wavelength of the X-rays. The XRD data for all the samples was produced and collected using a Shimadzu X-ray diffractometer (XRD, CuKα1 λ = 1.5406 Å), shown in **Figure 2.3**.

Figure 2.3- Shimadzu X-Ray Diffractometer.

2.3.2 SEM & EDS

SEM, as opposed to optical microscopy, allows for the observation of a material's surface morphology at the microscopic level. In this process, a focused beam of electrons acts to scan the sample. These electrons impact the sample, and then scatter to reveal information about the sample's constitution [25]. The information that can be derived from this process heavily depends on how the electrons scatter. Inelastically scattered electrons, known as secondary electrons, reflect to show the surface structure. Meanwhile, elastically scattered electrons, known as backscattered electrons, reflect from the inside of the sample and can be used to observe elemental details. Furthermore, deeply penetrative electrons result in X-ray radiation, which in turn provides identifying details about elemental type and distribution. EDS takes advantage of these unique X-ray signatures, generating a unique emission spectrum that can be used to approximate atomic weight distributions.

SEM and EDS data were collected using a SU5000 FE-SEM microscope, shown in **Figure 2.4**.

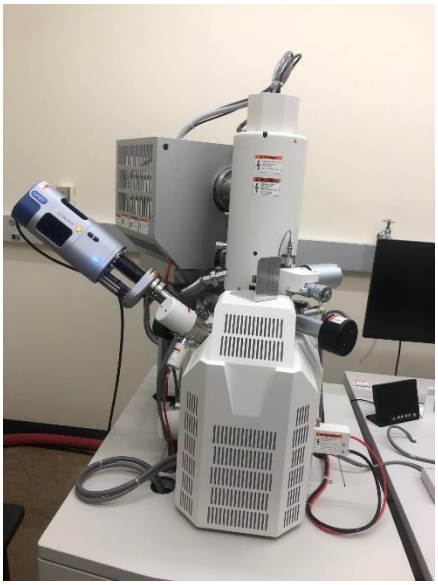

Figure 2.4- SU5000 FE-SEM microscope.

2.4 Electrochemical Characterization

The electrochemical properties of the various carbon aerogels were studied with the use of a PARSTAT MC electrochemical workstation (Princeton Applied Research, USA). These tests were carried out using a three-electrode system that consisted of a working electrode (the sample), a counter electrode (platinum wire coil), and a reference electrode (saturated calomel electrode). Additionally, an electrolyzer test was performed on a two-electrode system. The electrochemical testing setup, three-electrode system, and two-electrode system are visible in **Figure 2.5**. To prepare the samples for testing, the material (16 mg) was added to a mortar with PVDF binder (2 mg) and carbon black (2 mg). NMP (15 drops) was then added to the mixture, which was subsequently ground for 30 min each

to create an electrocatalytic ink. The resulting ink was applied to 5 precleaned nickel foam pieces, which were then dried in a vacuum oven at 60 °C for 48 hr. Electrochemical testing for the electrodes consisted of linear sweep voltammetry (LSV), electrochemical impedance spectroscopy (EIS), and chronoamperometry (CA). Each of these measurements was performed in 1 M KOH electrolyte.

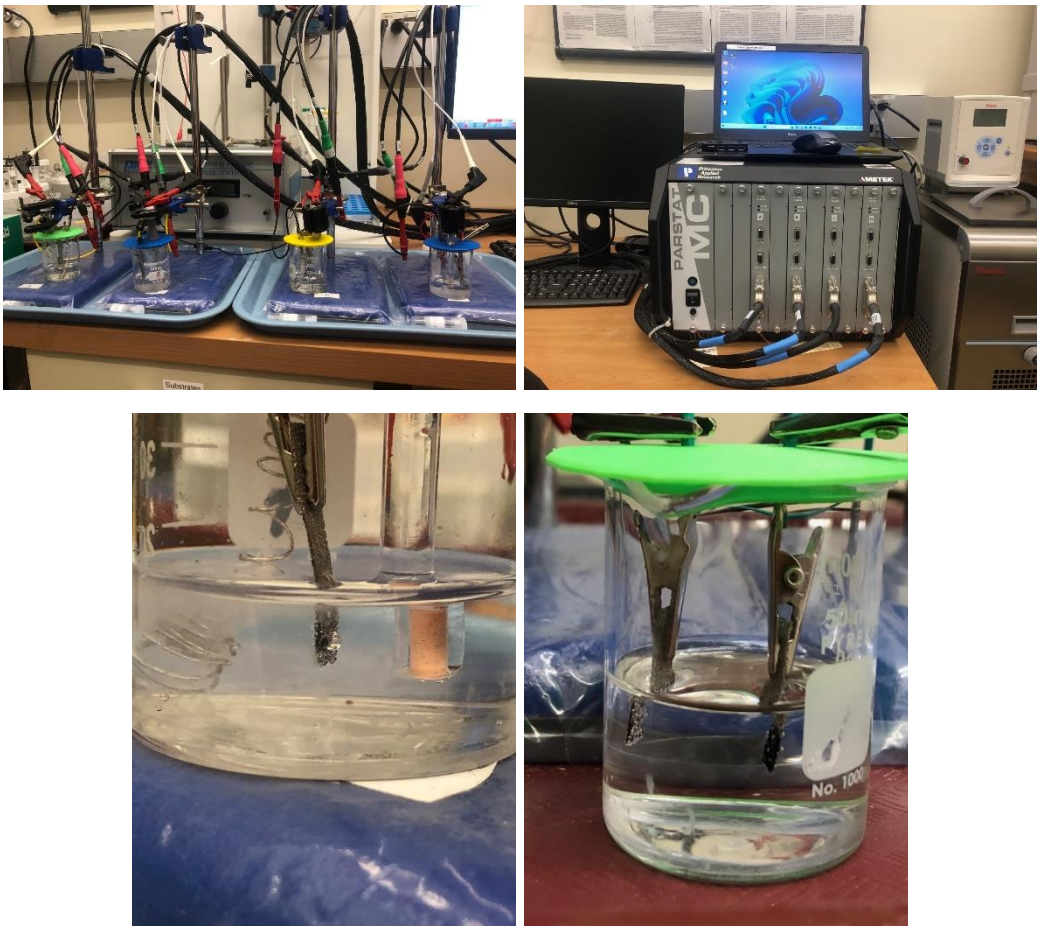

Figure 2.5- Electrochemical testing setup, alongside both three and two-electrode system.

CHAPTER III

RESULTS AND DISCUSSION

3.1. Structural characterization

3.1.1. XRD

XRD measurements of all samples were carried out within an angle range of 2θ = 15° to 80°. **Figure 3.1** shows the XRD spectra of RF-CCo, RF-CNi, and RF-CCoNi respectively. Each of the samples demonstrated peaks at 44.5° and 52°, which correspond to the (111) and (200) planes, respectively. Meanwhile, small peaks at 76.5° were observed in RF-CCoNi and RF-CNi. This peak corresponds to the (220) plane, and while a similar peak was expected in RF-CCo, it was likely lost in the noise due to RF-CCo's lower crystallinity. These three peaks are strongly indicative of both pure metallic cobalt and nickel, demonstrating that their metallic nature was preserved. Additionally, both results match with their respective JCPDS files, being No. 03-1051 for nickel and No. 15-0806 for cobalt respectively [26][27]. The broad peak at 26° indicates the formation of graphitic carbon, which was attributed to the metallic cobalt. This is due to the previously observed phenomenon of metallic cobalt acting as a graphitization catalyst for amorphous carbon at high heat [28]. **Figure 3.2** shows the XRD spectra of RF-CCoNi 25%-150%. Each of these spectra demonstrates the expected peak values, with the changes in peak intensity

corresponding to the changes in metal concentration. Finally, **Figure 3.3** provides the XRD spectra for RF-CCoNi 10%-40%, also demonstrating the expected changes in peak intensity. Altogether, these results establish that the peak intensity of the various RF-CCoNi samples correlate to the change in total metal concentration. Furthermore, the minimal number of peaks observed shows that the metals in these samples are in their base metallic form, as these material's oxides and hydroxides would coincide with the observation of many additional peaks. Finally, the observation of the Ni and Co (111) plane was important in the scope of electrochemistry, as it has been observed as an important active site for water splitting [29][30][31].

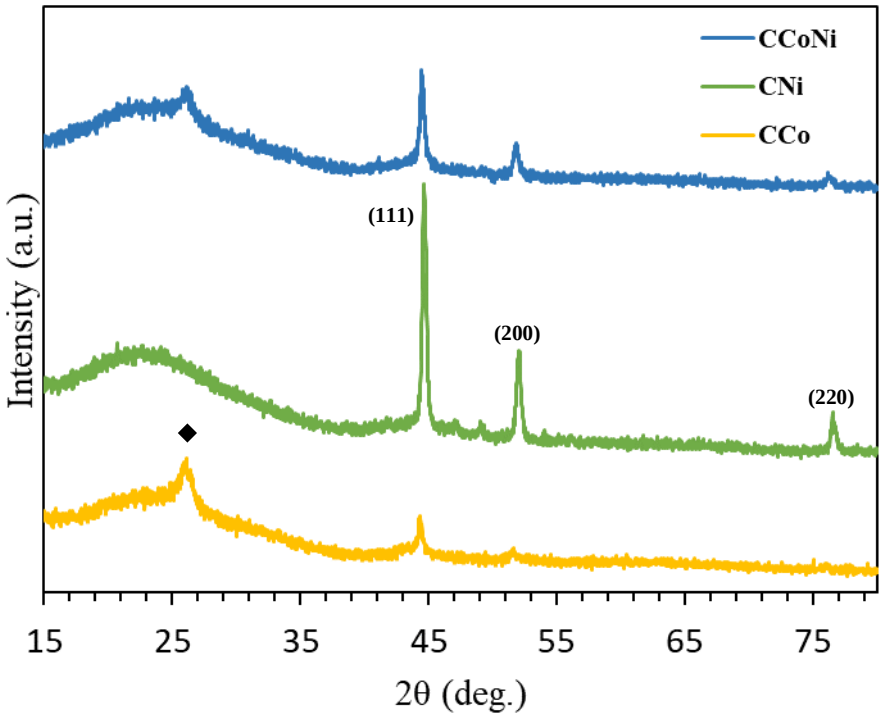

Figure 3.1- XRD spectra of RF-CCo, RF-CNi, and RF-CCoNi.

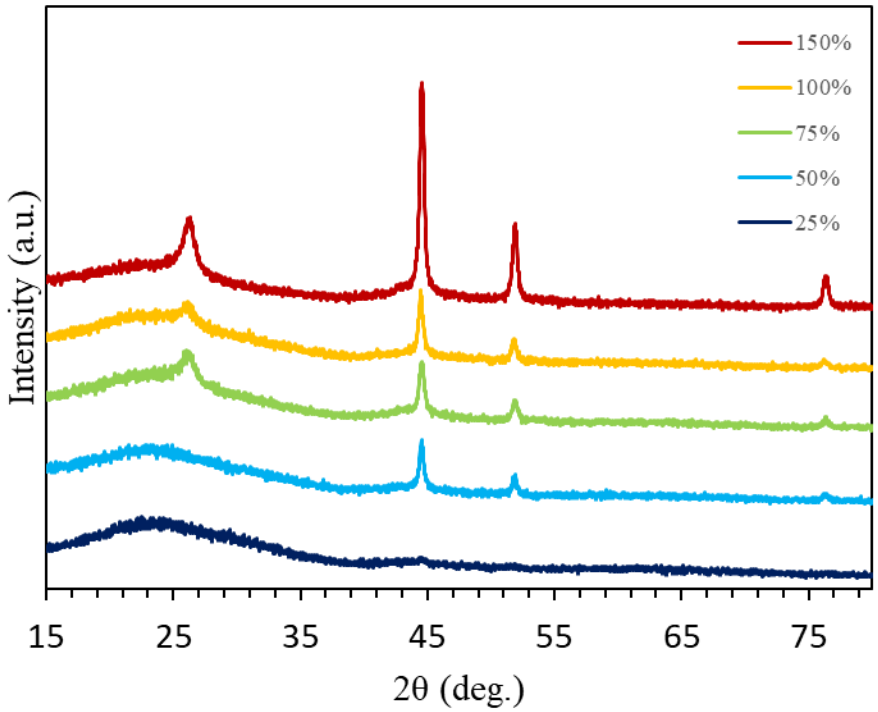

Figure 3.2- XRD spectra of RF-CCoNi 25%-150%.

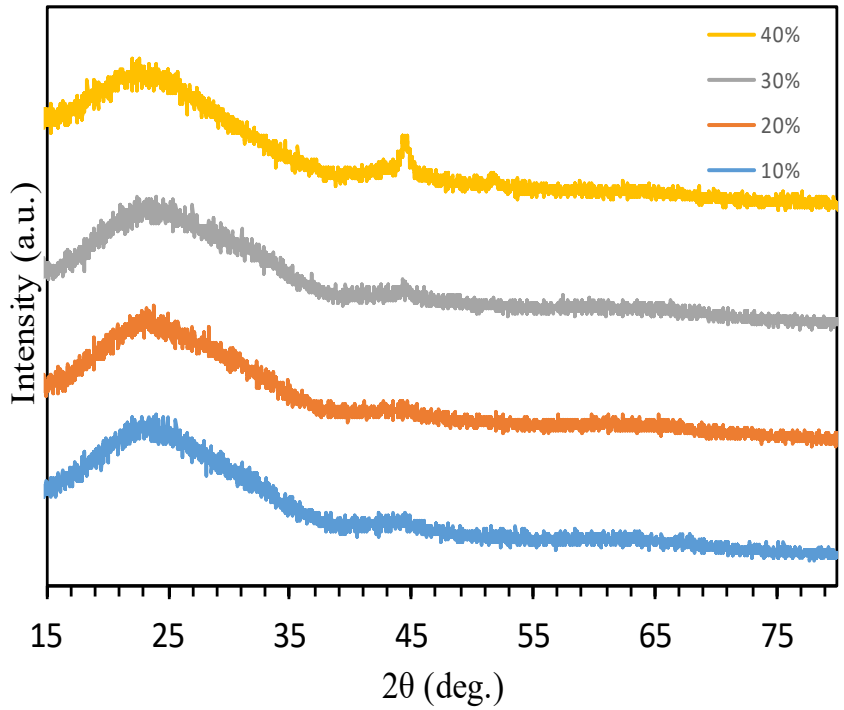

Figure 3.3- XRD spectra of RF-CCoNi 10%-40%.

3.1.2. SEM & EDS

SEM testing was performed on all samples to observe their microstructure, alongside EDS to measure elemental distribution. As shown in **Figure 3.3**, the addition of metal acetate to the RF-gel synthesis had a major effect on this final material's structure. RF-C possessed a plate-like structure reminiscent of graphene. This arrangement was to be expected, matching similar examples in literature. RF-CCo, meanwhile, produced notable agglomerations that ranged from 1-10 μm in diameter. RF-CCo and RF-CCoNi yielded similar patterns to each other, consisting of smaller, finely distributed nanoparticulate nodules. EDS analysis of these materials demonstrated an even distribution of carbon, oxygen, and the respective metals in each of the samples, with **Figure 3.4**, elucidating the individual element distributions for RF-CCoNi. In addition to identifying the elemental characteristics of the samples, EDS allows for the estimation of individual elemental wt.% of the bulk material. For RF-C, the material was shown to be 90.4% carbon by mass, with oxygen accounting for the remaining 9.6%. RF-CCo meanwhile had carbon, oxygen, and cobalt providing wt.% of 91.9%, 5.3% and 2.8% respectively. RF-CNi, provided wt.% of 90.5% carbon, 2.1% oxygen, and 7.4% nickel. Finally, RF-CCoNi had carbon maintaining 91% of its weight, oxygen being 2.4% of its weight, and both metals composing 3% of its weight each to a total of 6%. These results reveal that each of the samples were ~90% carbon by weight. Furthermore, the metal content varied between samples, but totals were observed to be similar between RF-CNi and RF-CCoNi. which was reflective of the morphological results observed in the SEM results. In total, it seemed that nickel and the CoNi mixture were better incorporated with

the aerogel synthesis, while cobalt by itself tended to agglomerate, with much of the unincorporated metal being lost between synthesis steps.

Figure 3.5 provides the SEM and EDS observations for RF-CCoNi 25%-150%. Herein it was observed that RF-CCoNi-25% retained most of the original aerogel's microstructure, with a distinct fuzziness provided by the growing metal nanoparticles. Opposingly, RF-CCoNi 50%,75%, and 150% recalled similar structures to RF-CCoNi, with the nodule size increasing commensurate with the metal content. EDS analysis again demonstrated that each of the constituent elements were well dispersed throughout the various samples. Weight % mapping of RF-CCoNi 25%-150% demonstrated mostly expected results. For RF-CCoNi 25% the C, O, Ni, and Co content was 94.7%, 3.4%, 0.9%, and 0.9% respectively. Notably, a trace amount of sulfur was detected in this sample, likely arising from trace sulfur compounds within the tube furnace during calcination, as it was absent from the other samples in this cohort. The remaining samples further fell in line with expected values and ratios, with the Co/Ni metal contents of RF-CCoNi 50%, 75%, and 150% being 1.8%/1.8%, 2.6%/2.8%, and 4.9%/4.7% each. These values align with the amount of metal added during synthesis, producing a linear relationship when compared.

Finally, **Figure 3.6** discerns the SEM and EDS observations for RF-CCoNi 10%-40%. RF-CCoNi 10% appears similar to RF-C, albeit slightly fuzzy. RF-CCoNi 20% maintained much of the original structure as well, with definite plates still clearly visible. RF-CCoNi 30% and RF-CCoNi 40% thereafter seemed to return the nodular trend established prior. EDS analysis of these samples again demonstrated an equal dispersity

of the expected metals in all the materials. For RF-CCoNi 10%-40%, the weight ratios were observed to be 0.4%/0.3%, 0.8%/0.8%, 0.9%/0.9%, and 1.2%/1.2% each.

These results establish a noticeable trend in nanocluster size that correlates with the amount of metal added. As the wt.% of metal increased, the size and definition of the nanoclusters did as well. Likely of greater importance is that as observed via EDS, the metals were well distributed throughout the samples. Furthermore, these metals were also approximated to be equal in wt.%, providing the desired 50/50 ratio for this experiment. These results, in conjunction with the XRD results and physical observations of the material, confirmed that the RF-CCoNi materials successfully integrated the metals into the carbon aerogel framework.

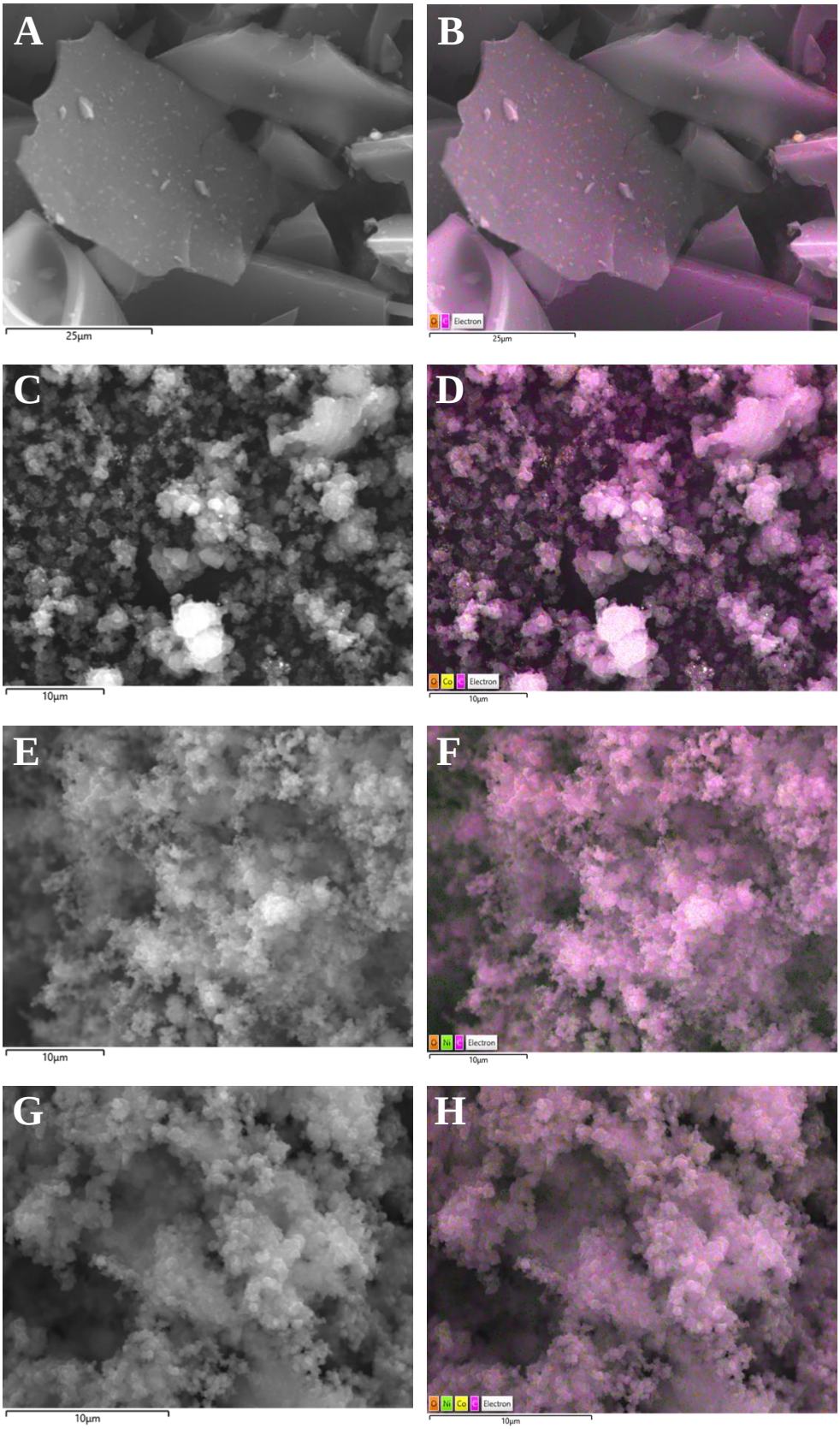

Figure 3.4- SEM & EDS images of RF-C, RF-CCo, RF-CCoNi, and RF-CCoNi.

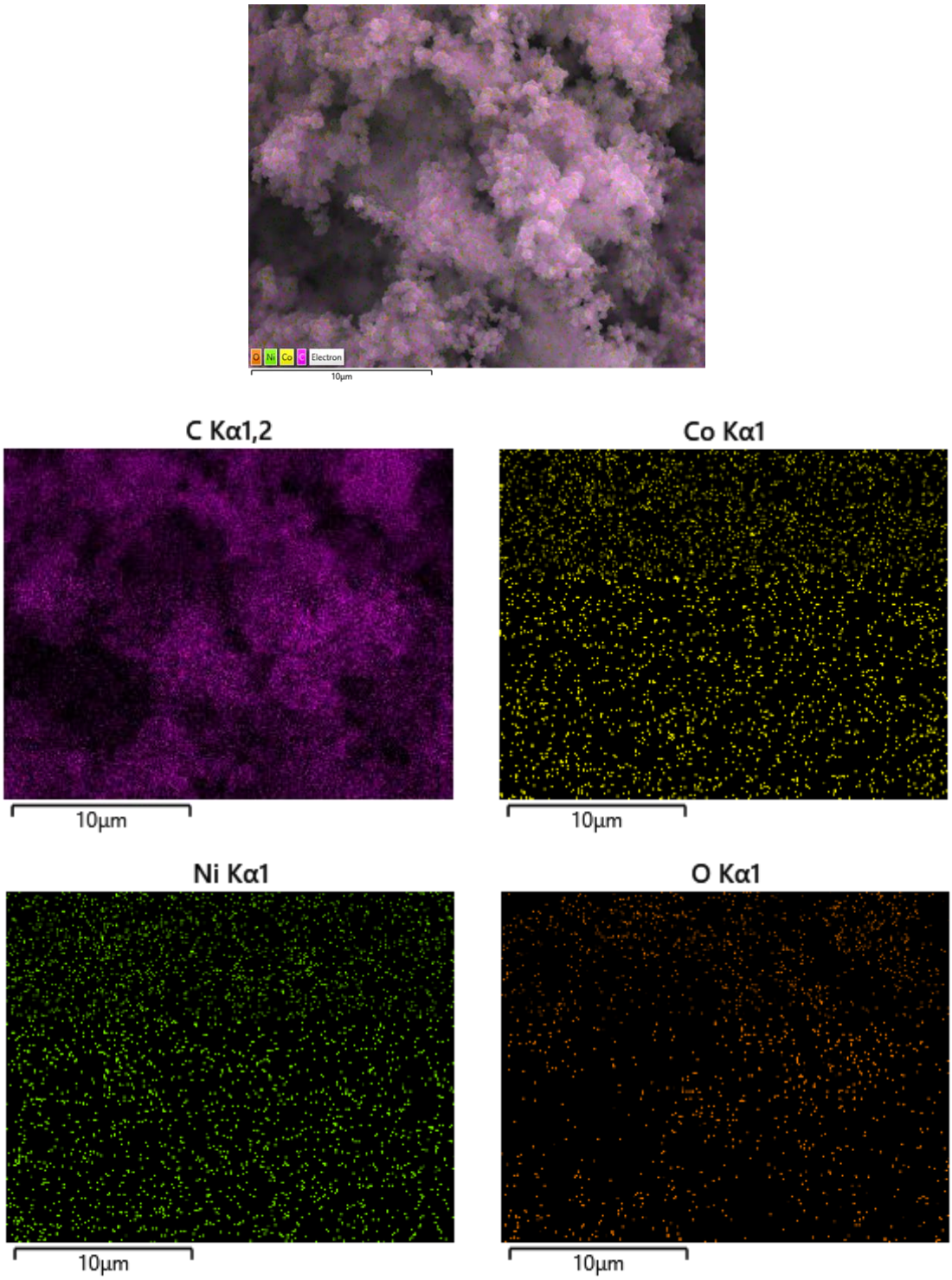

Figure 3.5- Individual elemental maps derived from EDS of RF-CCoNi.

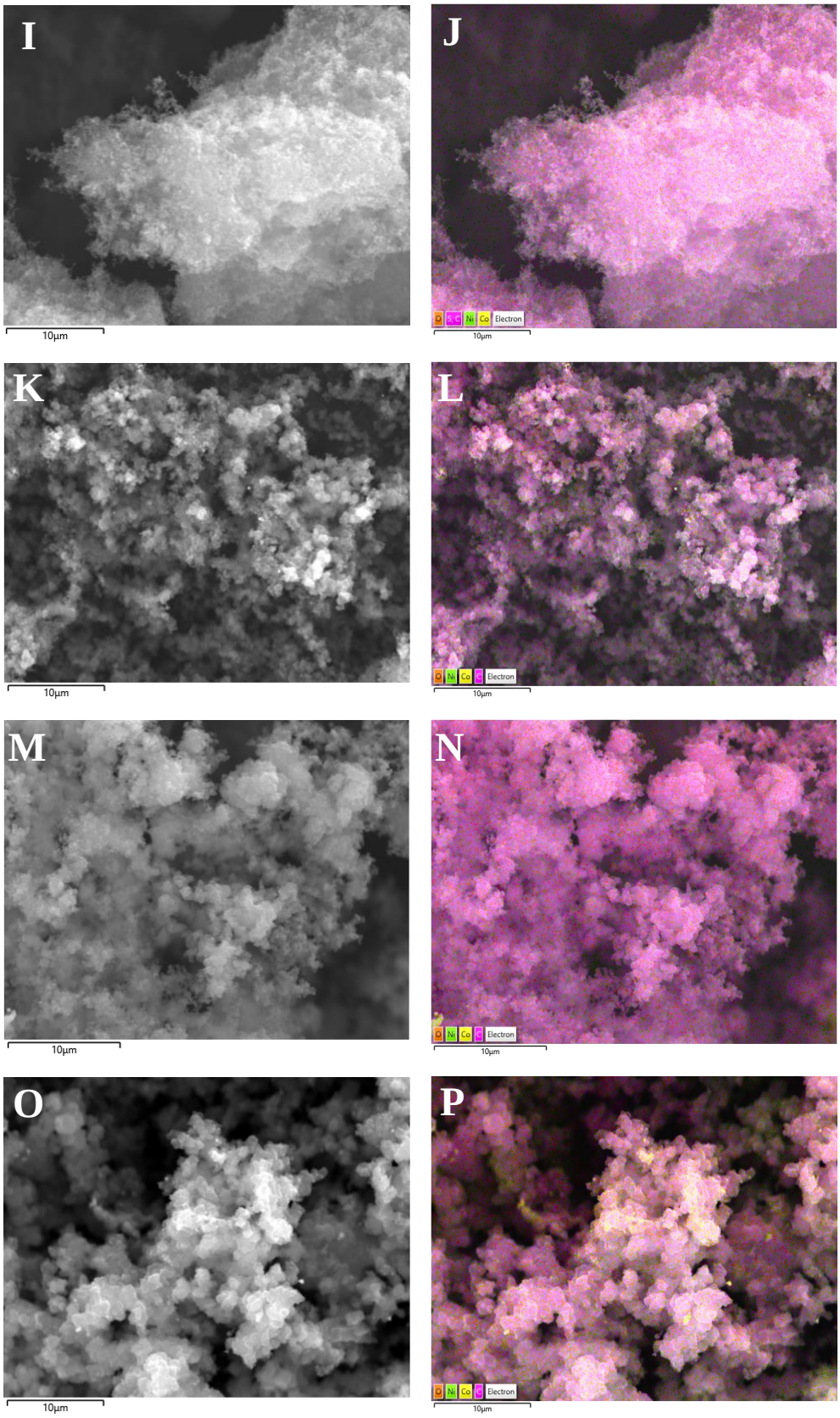

Figure 3.6- SEM & EDS images of RF-CCoNi 25%-150%.

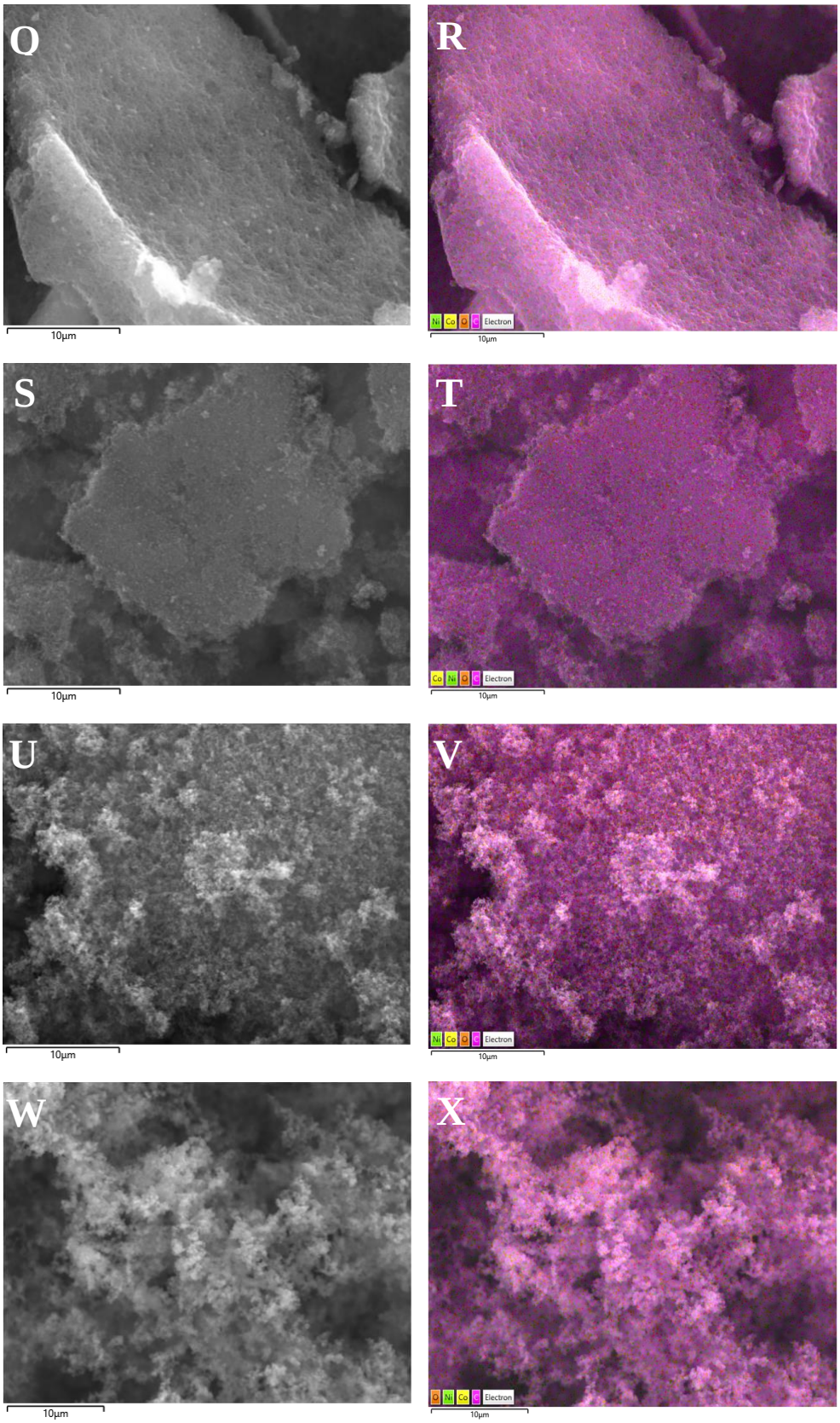

Figure 3.7- SEM & EDS images of RF-CCoNi 10%-40%.

3.2. Electrochemical measurements

3.2.1. Electrocatalytic performance for water splitting

LSV was performed to observe the OER activity of the developed electrodes. The resulting OER polarization curves were measured at a scan rate of 2 mV/s for each sample. **Figure 3.6** demonstrates the polarization curves of RF-C, RF-CCo, RF-CNi, RF-CCoNi, and RF-CCoNi 10%-150%. The observed overpotentials for RF-C, RF-CCo, RF-CNi, and RF-CCoNi were 320, 360, 330, and 310 mV respectively at 10 mA/cm^2. With RF-CCoNi demonstrating the most promising properties, further tests were performed to define the optimal ratio of metal to gel. As such, testing of RF-CCoNi 25%, RF-CCoNi 50%, RF-CCoNi 75%, and RF-CCoNi 150% demonstrated overpotentials of 310, 370, 360 and 360 mV, respectively at 10 mA/cm^2. With RF-CCoNi 25% providing comparable properties to RF-CCoNi, one final set of electrodes was tested. In this test, RF-CCoNi 10%, RF-CCoNi 20%, RF-CCoNi 30%, and RF-CCoNi 40% established overpotentials of 370, 320, 340, and 380 mV at 10 mA/cm^2. These results, alongside the upcoming Tafel slope values, verify that RF-CCoNi 25% exhibited the preferred balance of optimal OER activity and low metal content.

Tafel slopes for each of the electrodes were derived from the OER curves via the Tafel equation, $\eta = a + b \log j$. In this equation, η represents the overpotential, b the Tafel slope, and j the current density, with a being a constant. The OER Tafel slope values for each of the samples are shown in **Figure 3.7.** For RF-C, RF-CCo, RF-CNi, and RF-CCoNi, Tafel slope values were 79, 65, 65, and 47 mV/dec respectively. Furthermore, the Tafel slopes for RF-CCoNi 25%, RF-CCoNi 50%, RF-CCoNi 75%, and RF-CCoNi 150%, were

48, 56, 49, and 60 mV/dec respectively. Lastly, RF-CCoNi 10%, RF-CCoNi 20%, RF-CCoNi 30%, and RF-CCoNi 40% provided Tafel values of 59, 71, 53, and 55 mV/dec.

Figure 3.8 demonstrates the HER polarization curves for all the samples. LSV at a scan rate of 2 mV/s was performed to gather HER overpotential measurements. The HER overpotentials for RF-C, RF-CCo, RF-CNi, and RF-CCoNi were 236, 207, 202, and 141 mV at 10mA/g respectively. Again, With RF-CCoNi demonstrating the lowest overpotential, further testing was required. Thus, the HER overpotentials for RF-CCoNi 10%-150% were 204, 250, 188, 188, 149, 134, 158, and 140 mV respectively at 10 mA/g. These results, alongside the Tafel results, demonstrate that RF-CCoNi 50% provided optimal HER properties.

Tafel analysis obtained from the HER polarization curves showed slopes of 203, 168, 142, and 131 mV/dec for RF-C, RF-CCo, RF-CNi, and RF-CCoNi respectively. Further analysis of the slopes for RF-CCoNi 25%-150% provided values of 168, 147, 161, and 145 mV/dec each. Finally, RF-CCoNi 10%-40% showed Tafel values of 188, 157, 188, and 150 mV/dec. These results, alongside the HER curve results, demonstrate that RF-CCoNi 50% provided optimal HER properties.

EIS is a powerful and complex analytical tool that can yield vast amounts of information regarding electrode kinetics and interfacial properties. For this study, the properties of interest were the charge transfer resistance and electrolyte resistance. To collect this information, Nyquist plots were generated from 0.05 Hz to 10 kHz range at 0.6 V vs RHE at an AC amplitude of 10 mV for all samples, as seen in **Figure 3.11**. The resulting semicircular curves provide information about the electrolyte resistance, charge transfer resistance, and interfacial capacitance. These factors are hereafter represented as

R_s for electrode resistance, and R_{ct} for charge transfer resistance [32]. The charge transfer resistance can be derived from the diameter of the semicircle, with smaller diameters equating to lower charge transfer resistance. Meanwhile, the electrode resistance values are collected from the start point of the semicircle from zero. R_s was observed at ~3 Ω for RF-C, ~3.5 Ω for RF-CCo, ~1 Ω for RF-CNi, and ~2.5 Ω for RF-CCoNi. R_{ct} for these same samples were 6.2 Ω, 9.1 Ω, 2.3 Ω, and 3.1 Ω respectively. The extra hump observed in RF-C and those with a metal content below 40% is due to added electrolyte resistance at the electrode interface, arising from the hydrophobicity native to high carbon content [33]. In this regard, RF-CNi demonstrated the lowest total resistance, with RF-CCoNi being close behind. R_s and R_{ct} for RF-CCoNi 25%-150% were ~2.25 Ω 2.4 Ω, ~3 Ω 3.4 Ω, ~5.75 Ω 3.3 Ω, and ~2.5 Ω 1.3 Ω each. Finally, RF-CCoNi 10%, 20%, and 30% had R_s values at ~2 Ω, with RF-CCoNi 40% having a lower R_s value of ~1.25 Ω. These values corresponded with R_{ct} values of 1.5 Ω, 1.2 Ω, 1.4 Ω, and 1.4 Ω respectively. Overall, R_{ct} and R_s trended downwards in correspondence with metal content, barring the unmodified RF-C.

Stability is amongst the most important factors that can be measured for electrocatalyst application. This is because electrocatalysts with a relatively short cycle life are both economically inviable and wasteful. To observe the stability of the samples, two tests were performed. The first set of tests compared the LSV polarization curves for both OER and HER after 1 and 1000 cycles. As demonstrated in **Figure 3.13** and **Figure 3.14**, each of the tested electrodes provided little change between the cycles, suggesting good stability. The second set of tests determined the long-term stability of the electrodes. This test, known as CA, plots the change in current density over time at a set voltage (0.6

V vs RHE). In testing, many of the samples demonstrated only a slight loss in current density after 24 hours of testing. Additionally, stepwise changes observed in testing were due to the release of accumulated gas bubbles on the surface. These results suggest that the prepared electrodes had a relatively high stability during continuous use.

With these results in hand, the OER and HER properties were compared with other examples as seen in recent literature. As seen below, in **Table 3.1** RF-CCoNi 25% was compared to multiple bifunctional electrocatalysts, as well as a few monofunctional catalysts. In these comparisons, RF-CCoNi 25% was often superior in at least one field. For example, this material demonstrated enhanced properties when compared to porous 3D materials like carbon foam and other carbon aerogels. Meanwhile, this material demonstrated comparable reaction rates when compared to graphene-based materials, albeit with a higher comparable overpotential. It should be noted however that despite the loss in comparative overpotential, RF-CCoNi 25% had a much lower material cost alongside a less harsh synthesis method. In terms of HER properties, **Table 3.2**, compares RF-CCoNi 25% and RF-CCoNi 50% to many of the same bifunctional electrocatalysts of the former, as well as some dedicated HER electrocatalysts. In this application, both materials demonstrated fair properties, with RF-CCoNi 50% providing enhanced electrocatalytic properties. Again, RF-CCoNi 50% was only heavily outpaced by advanced materials containing graphene or noble metals.

Table 3.1- Comparison of OER activity vs other studies.

Sample ID	Type	Electrolyte	OER Overpotential (mV@10mA/cm^2)	Tafel Slope (mV/dec)	Reference
RF-CCoNi 25%	Carbon Aerogel	1 M KOH	310	48	**[This Work]**
CoNiP/CoNi-G/CMF	Graphene/ Carbon Foam	1 M KOH	341	58	[34]
Ni_3S_2– Co_9S_8/NCAs	Carbon Aerogel	1 M KOH	337	77	[35]
CoO_x/CN_x	Cobalt Oxide Nanosheet	1 M KOH	310	60.7	[36]
$CuFeS_2$@ rGO	CuFeS2 on graphene oxide	1 M KOH	176	216	[37]
N-VGSs@CB/CoP	CoP on graphene	1 M KOH	256	61	[38]
$Co_1Mo_1Ni_{0.5}Pi$	CoMo ternary phosphate	1 M KOH	272	84.71	[33]
ZnCo-C/CA-PANI@NF	ZnCo-C PANI Nanofibers	1 M KOH	338	42	[39]
Co-T-BPY	Co3S4 Nanoparticles	1 M KOH	285	109	[40]
HfCoS/rGO	HfCoS on r graphene oxide	1 M KOH	210	46	[41]

Table 3.2- Comparison of HER activity vs other studies.

Sample ID	Type	Electrolyte	HER Overpotential (mV@10mA/cm^2)	Tafel Slope (mV/dec)	Reference
RF-CCoNi 25%	Carbon Aerogel	1 M KOH	188	168	**[This Work]**
RF-CCoNi 50%	Carbon Aerogel	1 M KOH	134	147	**[This Work]**
CoNiP/CoNi-G/CMF	Graphene/ Carbon Foam	1 M KOH	224	85	[34]
CoO_x/CN_x	Cobalt Oxide Nanosheet	1 M KOH	365	168.6	[36]
$CuFeS_2$@ rGO	CuFeS2 on graphene oxide	1 M KOH	153	150	[37]
N-VGSs@CB/CoP	CoP on graphene	1 M KOH	114	86	[38]
$Co_1Mo_1Ni_{0.5}Pi$	CoMo ternary phosphate	1 M KOH	96	145.32	[33]
ZnCo-C/CA-PANI@NF	ZnCo-C PANI Nanofibers	1 M KOH	338	42	[39]
HfCoS/rGO	HfCoS on r graphene oxide	1 M KOH	164	49	[41]
MoS_2/CoS_2	MoS2/CoS2 Heterointerface	1 M KOH	67	70	[42]
Hcp RuNi	RuNi Nanoplates	1 M KOH	37	20	[43]

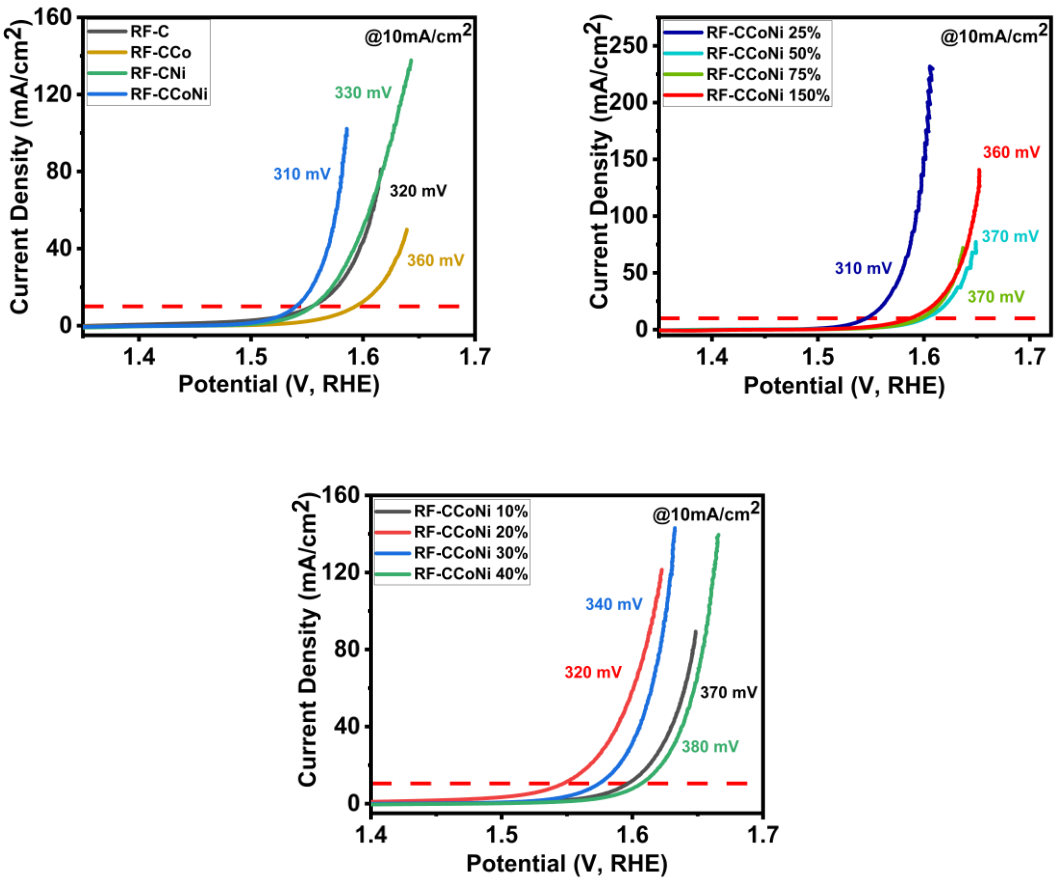

Figure 3.8- OER polarization curves of all electrodes.

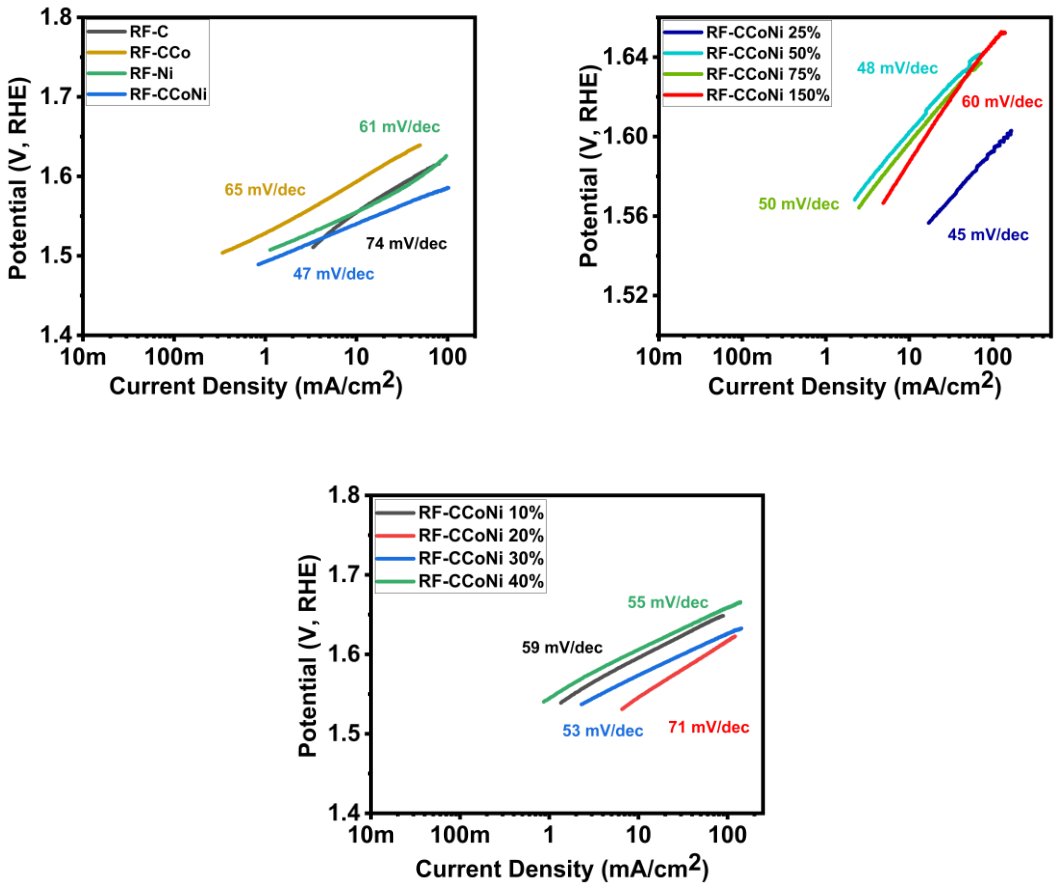

Figure 3.9- OER Tafel slopes of all electrodes.

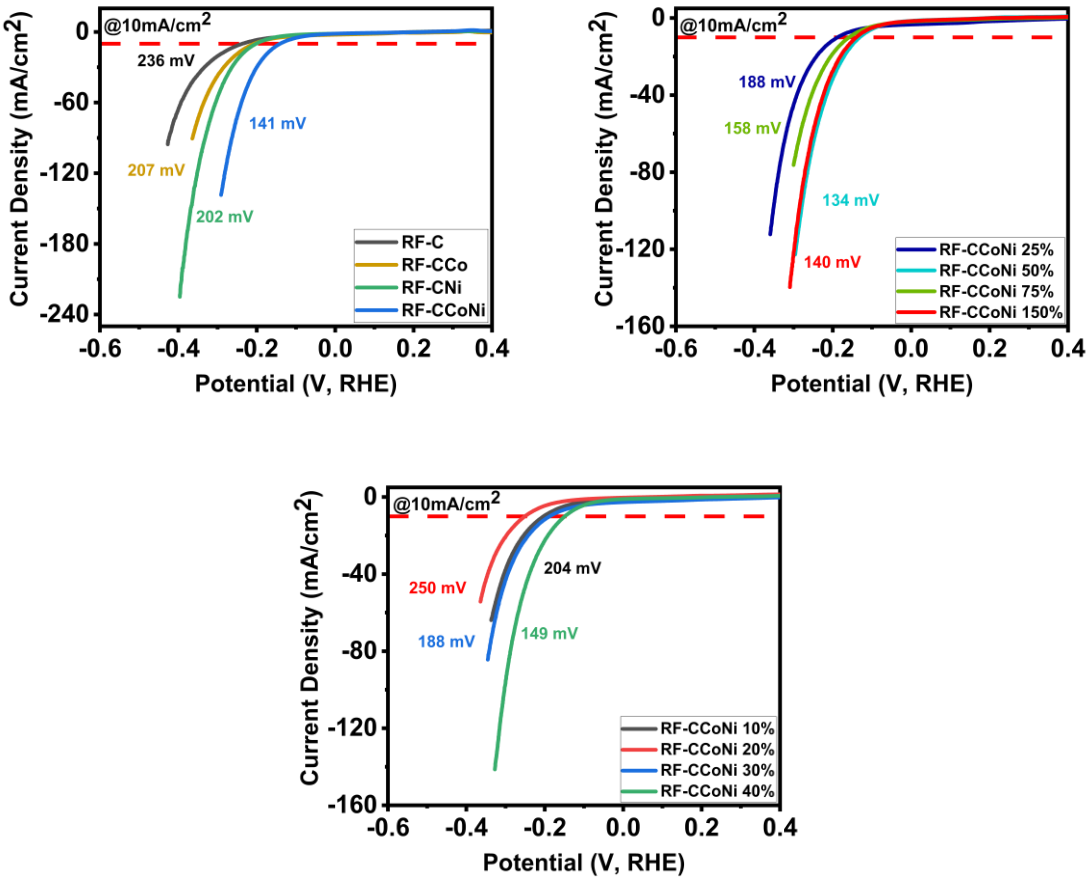

Figure 3.10- HER polarization curves of all electrodes.

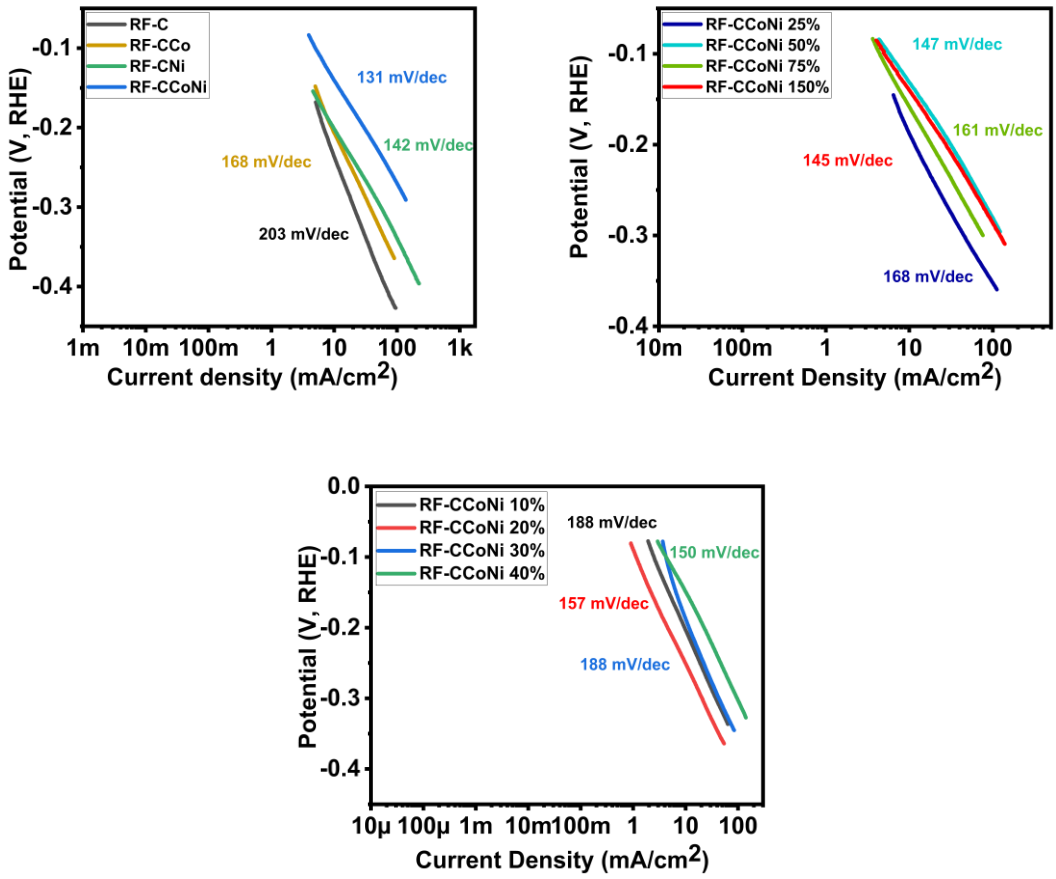

Figure 3.11- HER Tafel slopes of all electrodes.

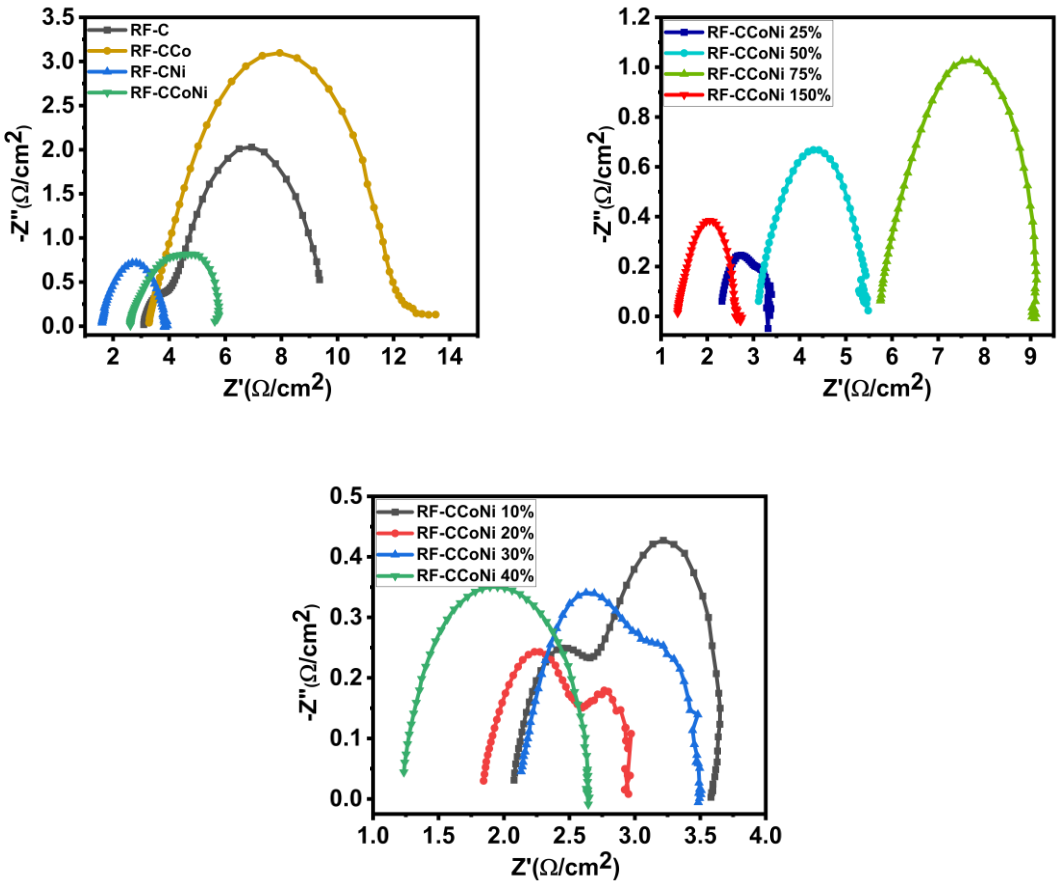

Figure 3.12- Nyquist plots of all electrodes.

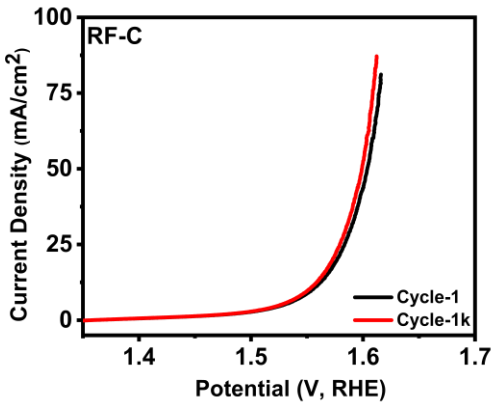
RF-C
Current Density (mA/cm2)
Potential (V, RHE)
Cycle-1
Cycle-1k

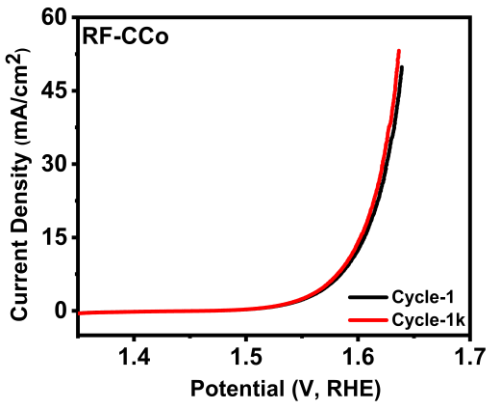
RF-CCo
Current Density (mA/cm2)
Potential (V, RHE)
Cycle-1
Cycle-1k

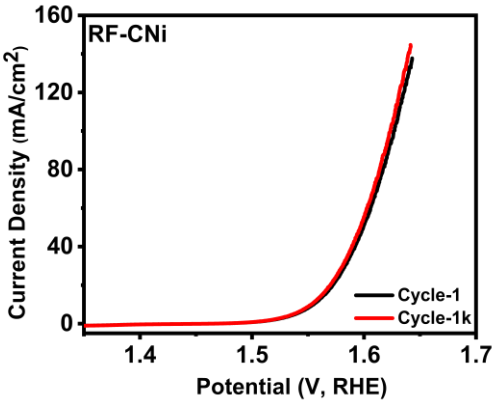
RF-CNi
Current Density (mA/cm2)
Potential (V, RHE)
Cycle-1
Cycle-1k

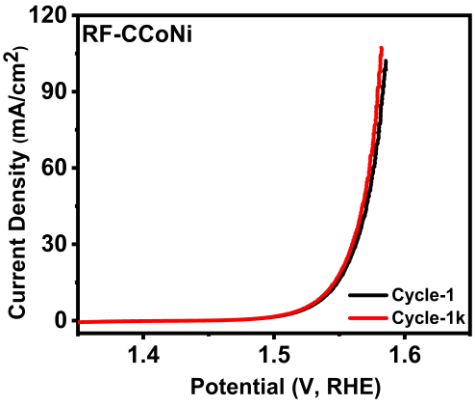
RF-CCoNi
Current Density (mA/cm2)
Potential (V, RHE)
Cycle-1
Cycle-1k

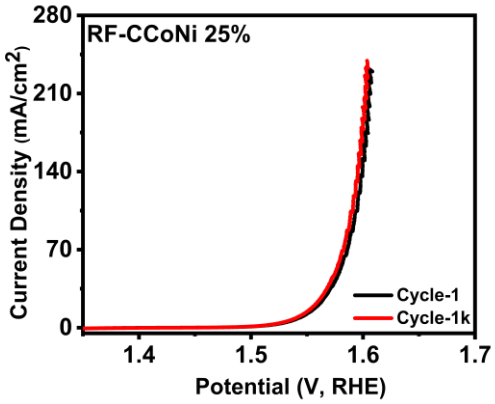
RF-CCoNi 25%
Current Density (mA/cm2)
Potential (V, RHE)
Cycle-1
Cycle-1k

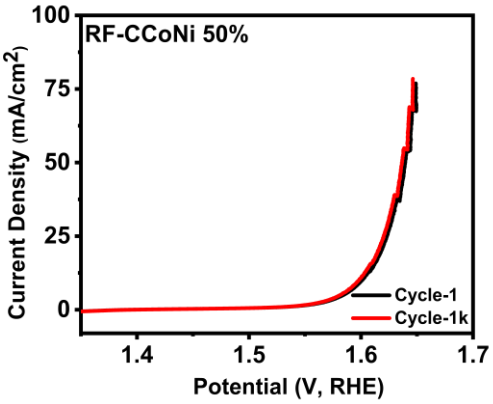
RF-CCoNi 50%
Current Density (mA/cm2)
Potential (V, RHE)
Cycle-1
Cycle-1k

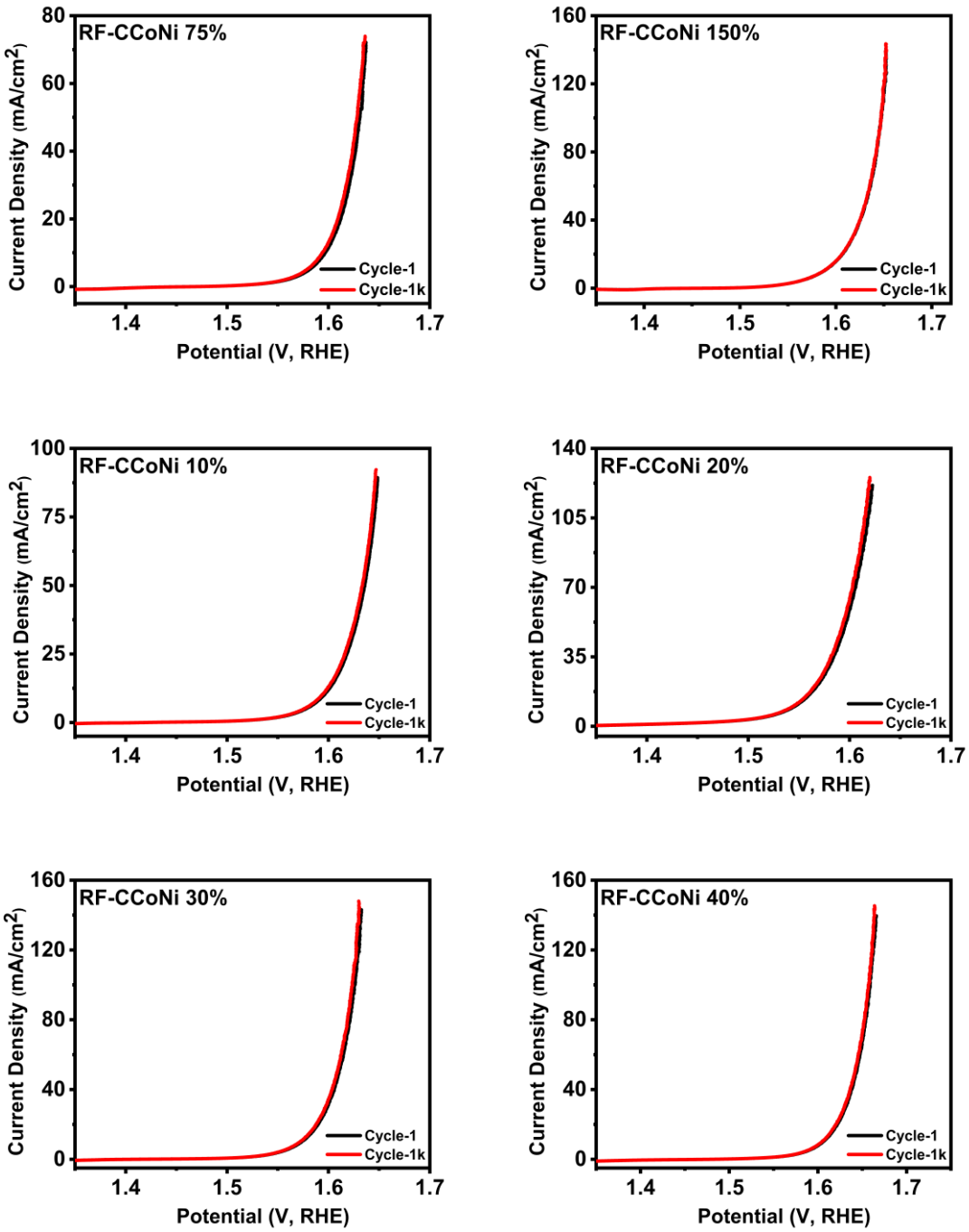

Figure 3.13- 1 vs 1k OER polarization curves of all electrodes.

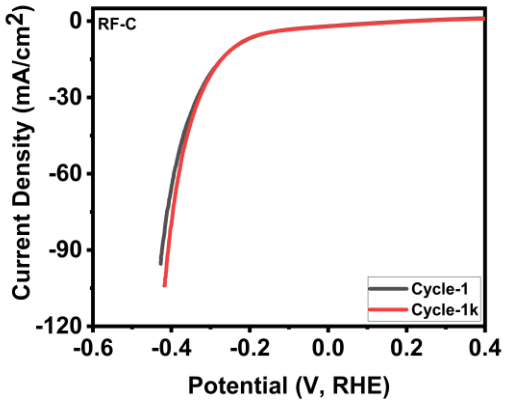
RF-C
Current Density (mA/cm2)
Potential (V, RHE)
Cycle-1
Cycle-1k

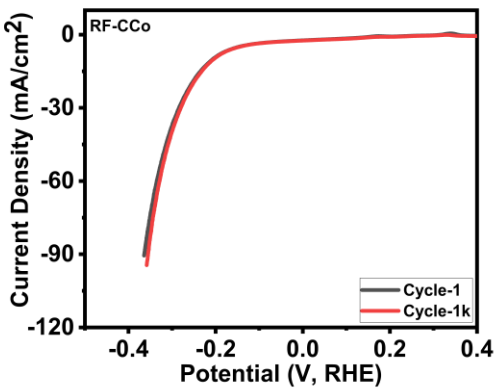
RF-CCo
Current Density (mA/cm2)
Potential (V, RHE)
Cycle-1
Cycle-1k

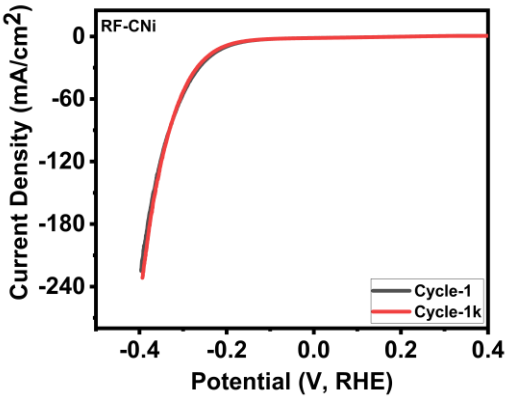
RF-CNi
Current Density (mA/cm2)
Potential (V, RHE)
Cycle-1
Cycle-1k

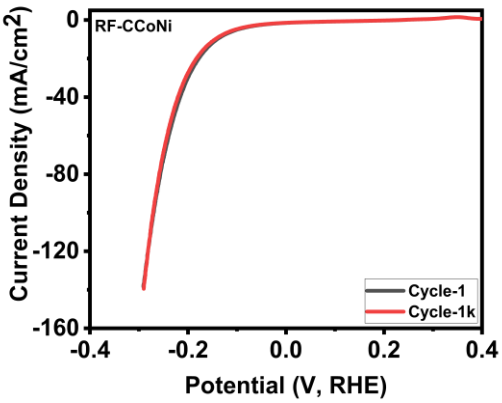
RF-CCoNi
Current Density (mA/cm2)
Potential (V, RHE)
Cycle-1
Cycle-1k

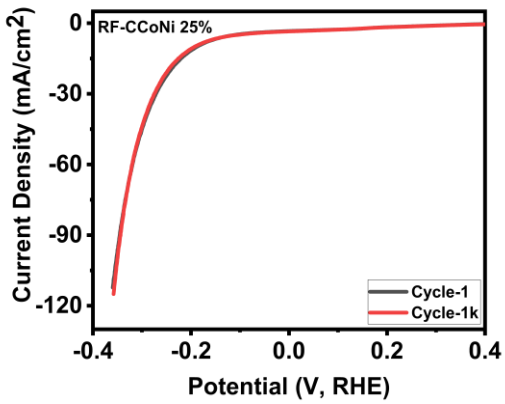
RF-CCoNi 25%
Current Density (mA/cm2)
Potential (V, RHE)
Cycle-1
Cycle-1k

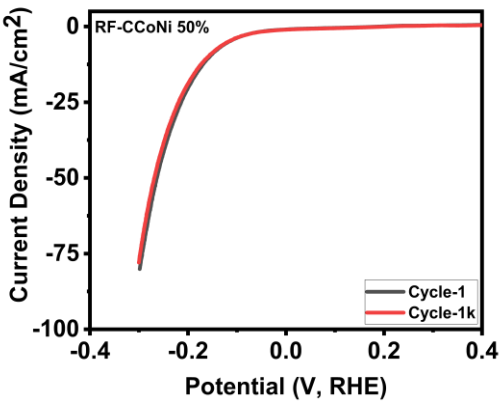
RF-CCoNi 50%
Current Density (mA/cm2)
Potential (V, RHE)
Cycle-1
Cycle-1k

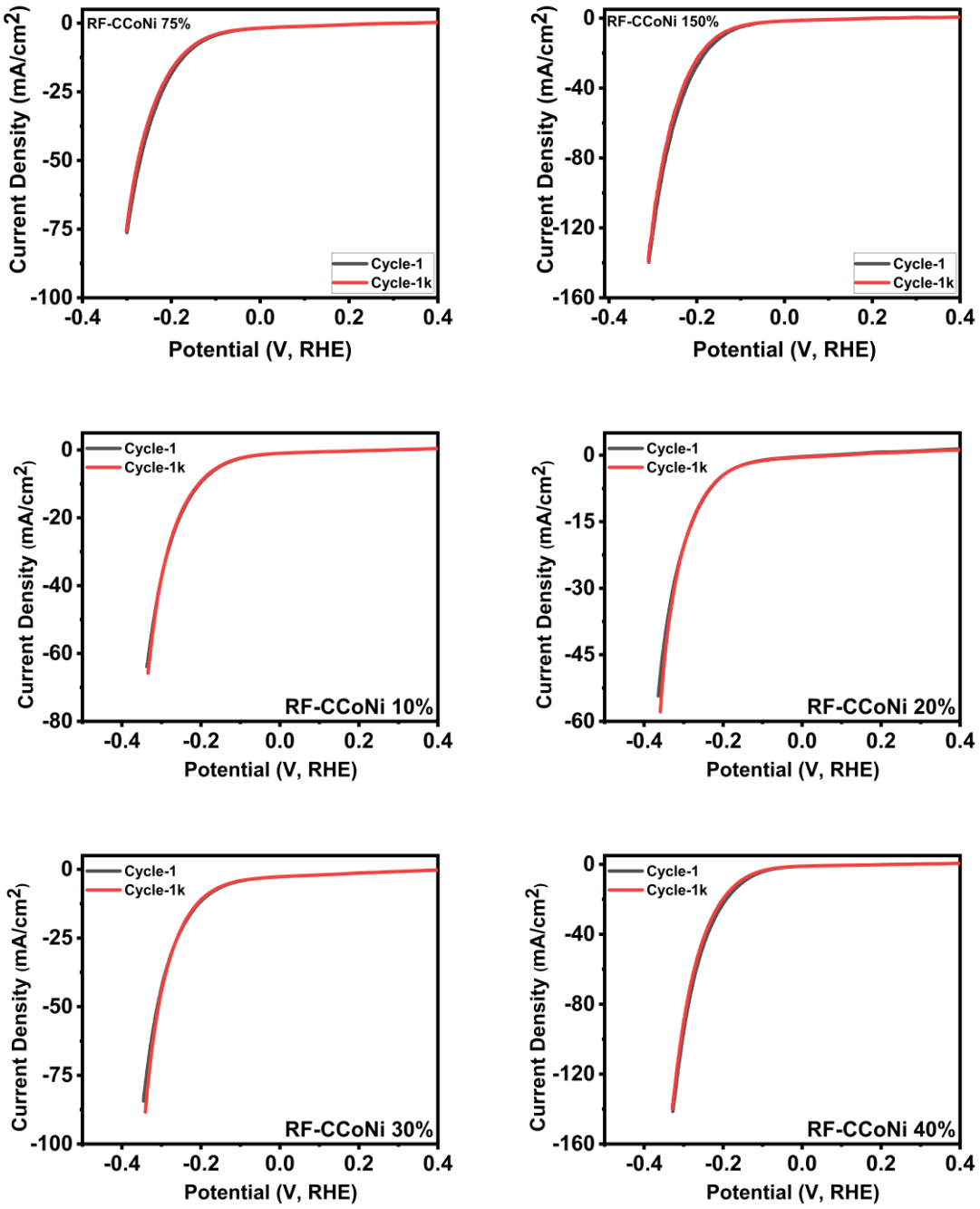

Figure 3.15- 1 vs 1k HER polarization curves of all electrodes.

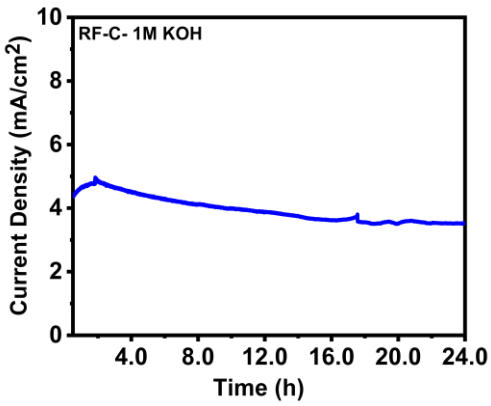
RF-C- 1M KOH
Current Density (mA/cm2)
Time (h)

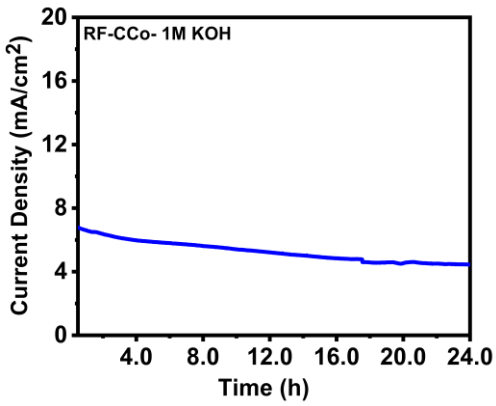
RF-CCo- 1M KOH
Current Density (mA/cm2)
Time (h)

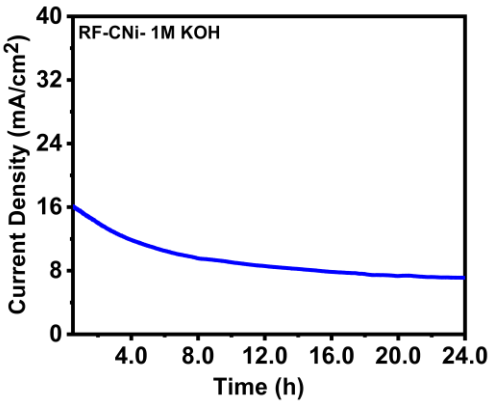
RF-CNi- 1M KOH
Current Density (mA/cm2)
Time (h)

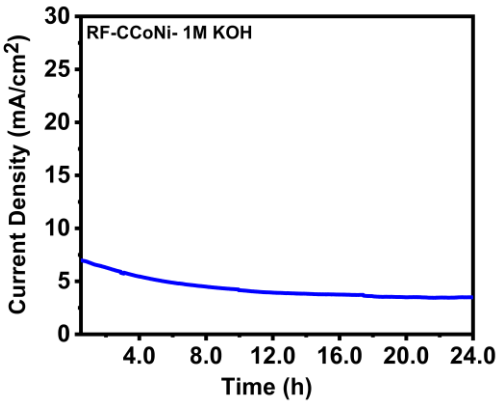
RF-CCoNi- 1M KOH
Current Density (mA/cm2)
Time (h)

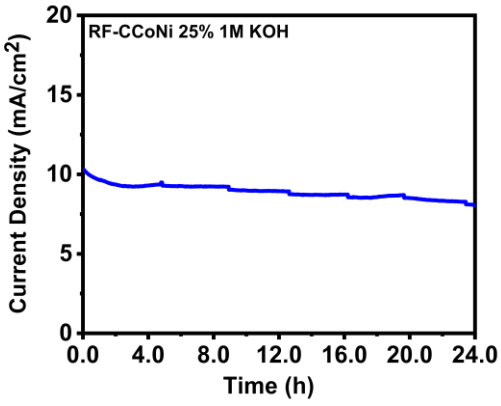
RF-CCoNi 25% 1M KOH
Current Density (mA/cm2)
Time (h)

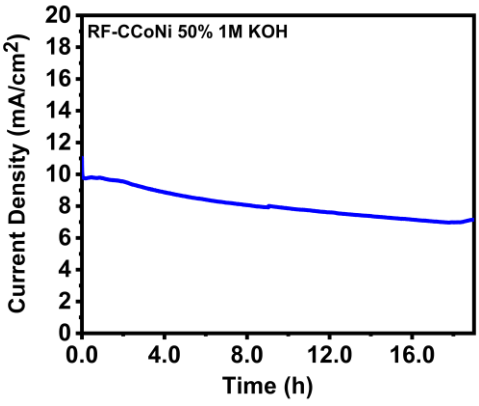
RF-CCoNi 50% 1M KOH
Current Density (mA/cm2)
Time (h)

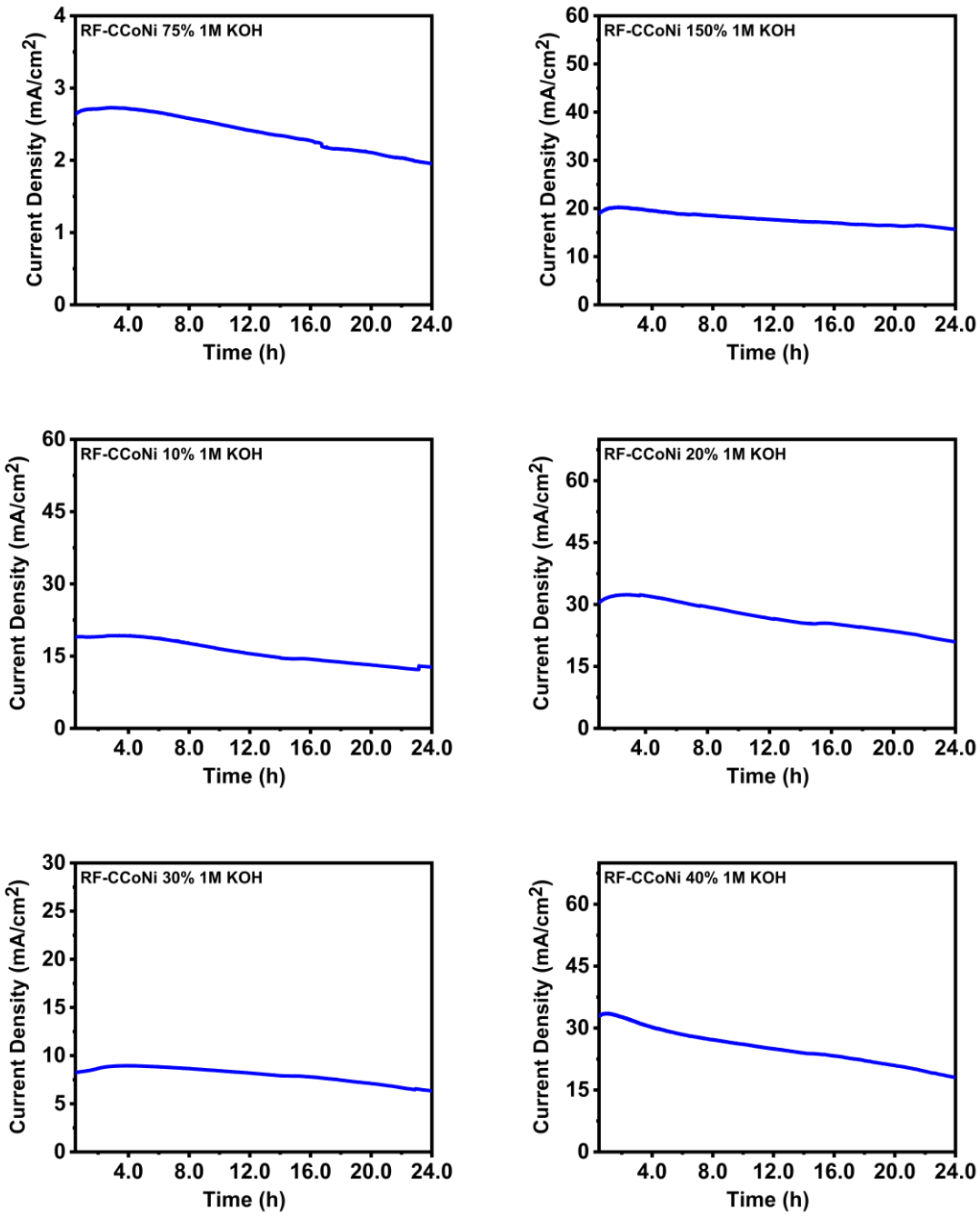

Figure 3.15- Chronoamperometry of all electrodes.

3.2.2. Electrocatalytic properties for electrolyzer

Given the promising results of the independent HER/OER trials, a two-electrode mock electrolyzer experiment was conducted. This trial provides information for the electrocatalysts under applicatory conditions. For this portion of the experiment, RF-CCoNi 25% and RF-CCoNi 50% were selected for their selectivity for OER and HER respectively. Much like the three electrode trials, this experiment used 1 M KOH as the electrolyte, with LSV and CA being used to characterize the sample. **Figure 3.17** provides the cell potential data and stability of the as-constructed electrolyzer. In this, the onset cell potential of the reaction was observed to be 1.60 V at the benchmark current density of 10 mA/cm^2. Furthermore, the cell demonstrated good stability, with a drop of 1 mA/cm^2 after 24 hr of operation. Furthermore, almost no change was detected in LSV 1 vs 1k, again demonstrating the material's high stability. As seen in **Table 3.3**, this electrolyzer possessed comparable electrical potentials to other examples at 10 mA/cm^2. As such, RF-CCoNi 25%/50% is a competitive option as an electrolyzer when compared to other studies.

Table 3.3- Comparison of electrolyzer results vs other studies.

Sample ID	Type	Electrolyte	Potential ($V@10mA/cm^2$)	Reference
RF-CCoNi 25%/50%	Carbon Aerogel	1 M KOH	1.60	**[This Work]**
N-VGSs@CB/CoP	Cobalt Phosphide Nanoparticles	1 M KOH	1.60	[38]
Ni/MoC/Ti_3C_2Tx@C	Carbon-Encapsulated Multimetallic Hybrid	1 M KOH	1.64	[44]
MoS_2/NiS_2	Multimetallic Sulfide	1 M KOH	1.51	[45]
V_2CTx/Ag-NPs	Ag Nanoparticle-Decorated MXene	1 M KOH	1.60	[46]

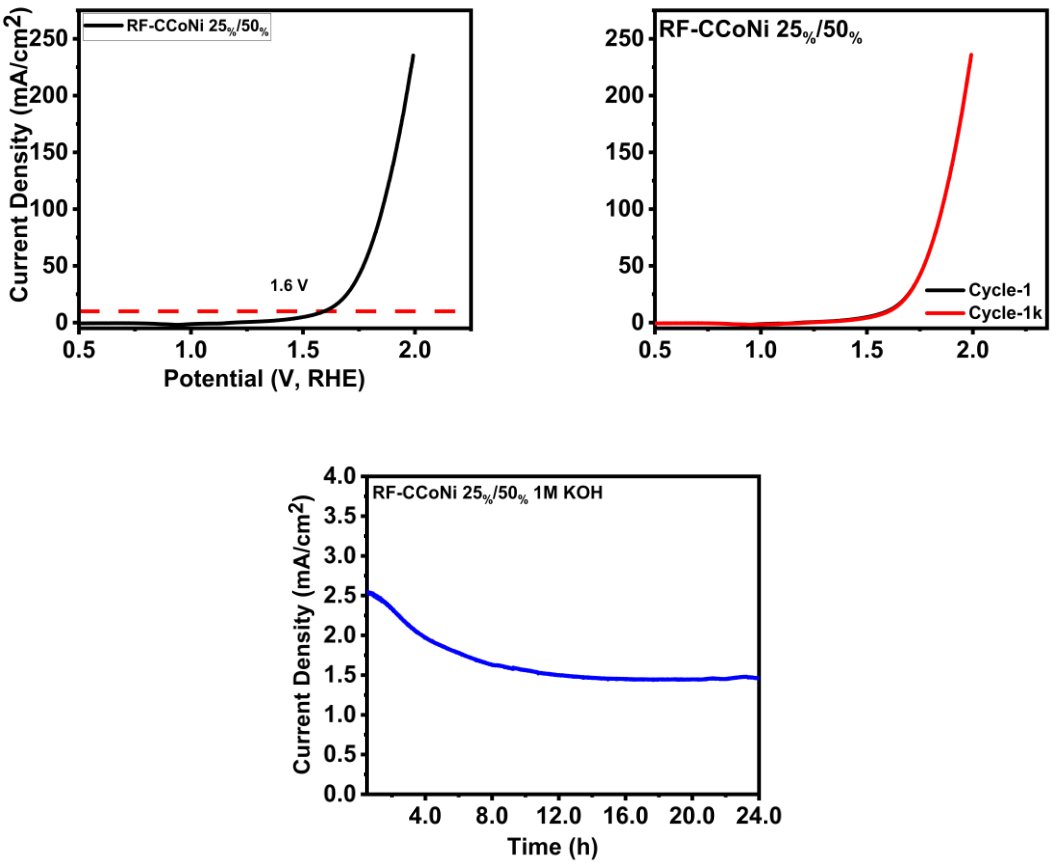

Figure 3.16- Electrolyzer polarization curve, alongside 1 vs 1k and CA stability tests.

CHAPTER IV

CONCLUSION

4.1 Conclusion

In this study, a metal-inclusive carbon aerogel was designed and optimized for low cost and high electrocatalytic activity. These materials were derived from the same RF aerogel synthesis, with their ratio of cobalt and nickel optimized for overall water splitting. Of all the samples developed, RF-CCoNi 25% demonstrated the most optimal properties. First and foremost, it maintained a majority of the aerogel superstructure, which was often lost past RF-CCoNi 30%. Furthermore, RF-CCoNi 25% demonstrated similar electrochemical properties to RF-CCoNi, indicating the benefits of maintaining this structure, even with the reduced metal content. In terms of actual electrocatalytic activity, RF-CCoNi demonstrated superior OER performance, with a low overpotential of 310 mV alongside a Tafel slope of 45 mV/dec. Meanwhile, RF-CCoNi 25% demonstrated a HER overpotential of 188 mV with a Tafel slope of 168 mV/dec. However, it should be noted that, unlike the OER overpotential, HER overpotential tended to be lower with an increase in metal content, with RF-CCoNi 50% demonstrating an overpotential of 134 mV, likely due to emergent crystallite formation. EIS analysis demonstrated that charge transfer resistance generally decreased alongside metal content, again showing the benefits of maintaining the aerogel structure alongside metal inclusion. Finally, all the samples

demonstrated solid stability, with RF-CCoNi 25% maintaining most of its current density after 24 hours of CA. With these results in hand, further testing of the material in a two-electrode electrolyzer system was performed. This electrolyzer, made from RF-CCoNi 25% and RF-CCoNi 50%, demonstrated a low onset potential of 1.6 V at 10 mA/cm^2, with decent stability after 24 hr.

4.2 Future Work

Thanks to the nature of electrochemical experimentation, this work is open to many avenues of further experimentation. First and foremost, the amount of added metal could be further narrowed down to further discern the most optimal amount of metal acetate to add. Furthermore, the mass ratio of metal to cobalt could be altered. While the current ratio is 1:1, it could easily be adjusted to be 2:1 or 1:2, likely affecting electrochemical properties. Another option could be to add other metals to RF aerogel synthesis, with iron and copper being particularly notable due to their desirable electrochemical properties. One interesting option could be to change the gel, with bio-based gels such as cellulose or chitosan being particularly promising. Beyond modifying the initial material, further research could apply RF-CCoNi to different electrochemical reactions. Urea oxidation is an attractive application that could allow for water splitting at a lower energy potential in dirty water, albeit with CO_2 as a byproduct. Another option could be to apply this material as a methanol oxidation catalyst, allowing it to be used in a direct methanol fuel cell. Considering the above, RF-CCoNi and its potential derivatives provide many avenues for further work and research.

REFERENCES

[1] R.E. Smalley, Future Global Energy Prosperity: The Terawatt Challenge, MRS Bull. 30 (2005) 412–417.

[2] K.O. Yoro, M.O. Daramola, Chapter 1 - CO2 emission sources, greenhouse gases, and the global warming effect, in: M.R. Rahimpour, M. Farsi, M.A.B.T.-A. in C.C. Makarem (Eds.), Woodhead Publishing, 2020: pp. 3–28.

[3] W. Ostrowski, The Twenty Years' Crisis of European Energy Security: Central and Eastern Europe and the US, Geopolitics. 27 (2022) 875–897.

[4] Z. Zhu, T. Jiang, M. Ali, Y. Meng, Y. Jin, Y. Cui, W. Chen, Rechargeable Batteries for Grid Scale Energy Storage, Chem. Rev. 122 (2022) 16610–16751.

[5] C. Yang, Y. Lu, W. Duan, Z. Kong, Z. Huang, T. Yang, Y. Zou, R. Chen, S. Wang, Recent Progress and Prospective of Nickel Selenide-Based Electrocatalysts for Water Splitting, Energy & Fuels. 35 (2021) 14283–14303.

[6] T. Wollandt, S. Mangel, J. Kussmann, C.C. Leon, A. Scavuzzo, C. Ochsenfeld, K. Kern, S.J. Jung, Charging and Electric Field Effects on Hydrogen Molecules Physisorbed on Graphene, J. Phys. Chem. C. 127 (2023) 4326–4333.

[7] J. Samuel, S. Ok, Petroleum Asphaltene-Based Activated Nanoporous Carbon for CO2 Capture and H2 Storage, Ind. Eng. Chem. Res. 62 (2023) 9939–9950.

[8] Y. Cho, H. Cho, E.S. Cho, Nanointerface Engineering of Metal Hydrides for Advanced Hydrogen Storage, Chem. Mater. 35 (2023) 366–385.

[9] V.H. Dayan, R.L. Proffit, B. Rosen, Hydrogen leak and fire detection, a survey,

NASA, 1970.

[10] Y. Kim, S.E. Jun, G. Lee, S. Nam, H.W. Jang, S.H. Park, K.C. Kwon, Recent Advances in Water-Splitting Electrocatalysts Based on Electrodeposition, Materials (Basel). 16 (2023).

[11] M. Wang, L. Zhang, Y. He, H. Zhu, Recent advances in transition-metal-sulfide-based bifunctional electrocatalysts for overall water splitting, J. Mater. Chem. A. 9 (2021) 5320–5363.

[12] S.J. Kim, S.G. Jo, E.B. Lee, J.W. Lee, Morphology-Controlled Nickel Oxide and Iron–Nickel Oxide for Electrochemical Oxygen Evolution Reaction, ACS Appl. Energy Mater. 6 (2023) 8360–8367.

[13] H. Zhang, Y. Li, L. Deng, J. Zhong, Z. Zhang, Y. Zhang, C. Zhuang, Porous Carbon Aerogel Decorated with TiO2 Quantum Dots for Highly Improved Photocatalytic H2 Evolution, ACS Appl. Energy Mater. 6 (2023) 7274–7282.

[14] X. Liu, X. Yi, J. Zhang, X. Zhao, S. Liu, T. Wang, S. Cui, Synthetic Strategy for MnO2 Nanoparticle/Carbon Aerogel Heterostructures for Improved Supercapacitor Performance, ACS Appl. Nano Mater. 6 (2023) 14127–14135.

[15] H. He, Q. Liu, S.-D. Zhang, H.-B. Chen, Fabrication and Properties of Polyimide/Carbon Fiber Aerogel and the Derivative Carbon Aerogel, Ind. Eng. Chem. Res. 61 (2022) 3952–3961.

[16] P. Hu, J. Lyu, C. Fu, W. Gong, J. Liao, W. Lu, Y. Chen, X. Zhang, Multifunctional Aramid Nanofiber/Carbon Nanotube Hybrid Aerogel Films, ACS

NaNo. 14 (2020) 688–697.

[17] Z. Guo, P. Ren, F. Yang, T. Wu, L. Zhang, Z. Chen, S. Huang, F. Ren, MOF-Derived Co/C and MXene co-Decorated Cellulose-Derived Hybrid Carbon Aerogel with a Multi-Interface Architecture toward Absorption-Dominated Ultra-Efficient Electromagnetic Interference Shielding, ACS Appl. Mater. Interfaces. 15 (2023) 7308–7318.

[18] H. Zhuo, Y. Hu, Z. Chen, X. Peng, H. Lai, L. Liu, Q. Liu, C. Liu, L. Zhong, Linking Renewable Cellulose Nanocrystal into Lightweight and Highly Elastic Carbon Aerogel, ACS Sustain. Chem. Eng. 8 (2020) 11921–11929.

[19] Q. Luo, H. Zheng, Y. Hu, H. Zhuo, Z. Chen, X. Peng, L. Zhong, Carbon Nanotube/Chitosan-Based Elastic Carbon Aerogel for Pressure Sensing, Ind. Eng. Chem. Res. 58 (2019) 17768–17775.

[20] Z. Cheng, J. Li, B. Wang, J. Zeng, J. Xu, W. Gao, S. Zhu, F. Hu, J. Dong, K. Chen, Scalable and Robust Bacterial Cellulose Carbon Aerogels as Reusable Absorbents for High-Efficiency Oil/Water Separation, ACS Appl. Bio Mater. 3 (2020) 7483–7491.

[21] V. Rodríguez-Mata, J.M. González-Domínguez, A.M. Benito, W.K. Maser, E. García-Bordejé, Reduced Graphene Oxide Aerogels with Controlled Continuous Microchannels for Environmental Remediation, ACS Appl. Nano Mater. 2 (2019) 1210–1222.

[22] S. Jindal, R. Anand, N. Sharma, N. Yadav, D. Mudgal, R. Mishra, V. Mishra, Sustainable Approach for Developing Graphene-Based Materials from Natural

Resources and Biowastes for Electronic Applications, ACS Appl. Electron. Mater. 4 (2022) 2146–2174.

[23] X. Ji, Y. Zhong, C. Li, J. Chu, H. Wang, Z. Xing, T. Niu, Z. Zhang, A. Du, Nanoporous Carbon Aerogels for Laser-Printed Wearable Sensors, ACS Appl. Nano Mater. 4 (2021) 6796–6804.

[24] Y. Luo, Q. Wang, Y. Chen, J. Feng, L. Wang, Y. Jiang, L. Li, X. Xu, J. Feng, Mn–N3–O-Loaded Graphitic Carbon Aerogel for an Efficient Oxygen Reduction Reaction, ACS Sustain. Chem. Eng. 11 (2023) 8075–8083.

[25] M. Lam, C. Schwarz, R. Sharma, J. Donnelly, An Introduction to Scanning Electron Microscopy and Science Communication Skills for Undergraduate Chemistry Students, J. Chem. Educ. 100 (2023) 2802–2808.

[26] D. Bora, P. Bavdane, V. Dave, S. Sreenath, G. Sethia, A. Satpati, R. Nagarale, Fabrication of Alkaline Electrolyzer Using Ni@MWCNT as an Effective Electrocatalyst and Composite Anion Exchange Membrane, ACS Omega. 7 (2022) 15467–15477.

[27] X. Shi, Z. Xu, C. Han, R. Shi, X. Wu, B. Lu, J. Zhou, S. Liang, Highly Dispersed Cobalt Nanoparticles Embedded in Nitrogen-Doped Graphitized Carbon for Fast and Durable Potassium Storage, Nano-Micro Lett. 13 (2020) 21.

[28] S.J. Goldie, S. Jiang, K.S. Coleman, Cobalt nanoparticle catalysed graphitization and the effect of metal precursor decomposition temperature, Mater. Adv. 2 (2021) 3353–3361.

[29] E.M. Davis, A. Bergmann, C. Zhan, H. Kuhlenbeck, B.R. Cuenya, Comparative study of Co3O4(111), CoFe2O4(111), and Fe3O4(111) thin film electrocatalysts for the oxygen evolution reaction, Nat. Commun. 14 (2023) 4791.

[30] A.Y. Faid, A.O. Barnett, F. Seland, S. Sunde, Ni/NiO nanosheets for alkaline hydrogen evolution reaction: In situ electrochemical-Raman study, Electrochim. Acta. 361 (2020) 137040.

[31] X. Feng, S. Bian, N. Wang, F. Wang, H. Guan, X. Hao, M. Ma, X. Gao, Y. Chen, Nickel Nanowire Arrays with Preferential Orientation for Boosting Hydrogen Evolution Reaction Capability, J. Electrochem. Soc. 167 (2020) 106501.

[32] A.C. Lazanas, M.I. Prodromidis, Electrochemical Impedance Spectroscopy─A Tutorial, ACS Meas. Sci. Au. (2023).

[33] P. Viswanathan, K. Kim, In Situ Surface Restructuring of Amorphous Ni-Doped CoMo Phosphate-Based Three-Dimensional Networked Nanosheets: Highly Efficient and Durable Electrocatalyst for Overall Alkaline Water Splitting, ACS Appl. Mater. Interfaces. 15 (2023) 16571–16583.

[34] D. Wei, L. Chen, L. Tian, S. Ramakrishna, D. Ji, Hierarchically Structured CoNiP/CoNi Nanoparticle/Graphene/Carbon Foams as Effective Bifunctional Electrocatalysts for HER and OER, Ind. Eng. Chem. Res. 62 (2023) 4987–4994.

[35] X. Wang, Y. Yang, R. Wang, L. Li, X. Zhao, W. Zhang, Porous Ni3S2–Co9S8 Carbon Aerogels Derived from Carrageenan/NiCo-MOF Hydrogels as an Efficient Electrocatalyst for Oxygen Evolution in Rechargeable Zn–Air Batteries,

Langmuir. 38 (2022) 7280–7289.

[36] R. Samanta, R. Mishra, B.K. Manna, S. Barman, Two-Dimensional Amorphous Cobalt Oxide Nanosheets/N-Doped Carbon Composites for Efficient Water Splitting in Alkaline Medium, ACS Appl. Nano Mater. 5 (2022) 17022–17032.

[37] S. Swathi, R. Yuvakkumar, G. Ravi, M. Thambidurai, H.D. Nguyen, D. Velauthapillai, Ternary Copper Iron Sulfide Microflowers Anchored on Reduced Graphene Oxide for Water Splitting, ACS Appl. Nano Mater. 6 (2023) 6538–6549.

[38] Q. Wu, Y. Huang, J. Yu, Cobalt Phosphide Nanoparticles Supported by Vertically Grown Graphene Sheets on Carbon Black with N-Doping Treatment as Bifunctional Electrocatalysts for Overall Water Splitting, Energy & Fuels. (2023).

[39] M.W. Fazal, F. Zafar, M. Asad, F. Mohammad H. Al Sulami, H. Khalid, A.A. Abdelwahab, M.U. Ur Rehman, N. Akhtar, W.A. El-Said, S. Hussain, M.A. Shenashen, Zn and Co Loaded Porous C Decorated Electrospun Nanofibers as Efficient Oxygen Evolution Reaction for Water Splitting, ACS Appl. Energy Mater. 6 (2023) 2739–2746.

[40] N. Sahu, J.N. Behera, MOF-Derived Co3S4 Nanoparticles Embedded in Nitrogen-Doped Carbon for Electrochemical Oxygen Production, ACS Appl. Nano Mater. 6 (2023) 7686–7693.

[41] M. Itagi, D. Chauhan, Y.-H. Ahn, HfCoS/rGO Bifunctional Electrocatalysts for Efficient Water Splitting in Alkaline Media, Energy & Fuels. 37 (2023) 11298–11308.

[42] Y. Zhu, J. Yao, L. Bai, W. Zhang, W. Wang, X. Ma, L. Wu, Dense MoS2/CoS2 Heterointerfaces with Optimized Electronic Structure for Efficient Alkaline Hydrogen Evolution Reaction, ACS Appl. Energy Mater. 6 (2023) 2479–2488.

[43] M. Fang, Y. Ji, S. Geng, J. Su, Y. Li, Q. Shao, J. Lu, Metastable Metal–Alloy Interface in RuNi Nanoplates Boosts Highly Efficient Hydrogen Electrocatalysis, ACS Appl. Nano Mater. 5 (2022) 17496–17502.

[44] C. Xu, X. Yang, K. Feng, M. Zhang, L. Yang, S. Yin, Carbon-Encapsulated Multimetallic Hybrid Electrocatalyst for Overall Water Splitting and Urea Oxidation, ACS Appl. Energy Mater. 6 (2023) 1404–1412.

[45] N. Yu, H. Ke, H. Yu, X. Wu, S. Li, G. Chen, J. Wang, N. Cai, Y. Xue, F. Yu, Polysulfide-Induced Synthesis of Coral-Like MoS2/NiS2 Nanostructures for Overall Water Splitting, ACS Appl. Nano Mater. 6 (2023) 5136–5144.

[46] Z. Haider, S. Fatima, S.A. Zahra, H. Li, S.H.M. Jafri, F. Amin, S. Rizwan, Ag Nanoparticle-Decorated V2CTx MXene Nanosheets as Catalysts for Water Splitting, ACS Appl. Nano Mater. 6 (2023) 2374–2384.

APPENDIX

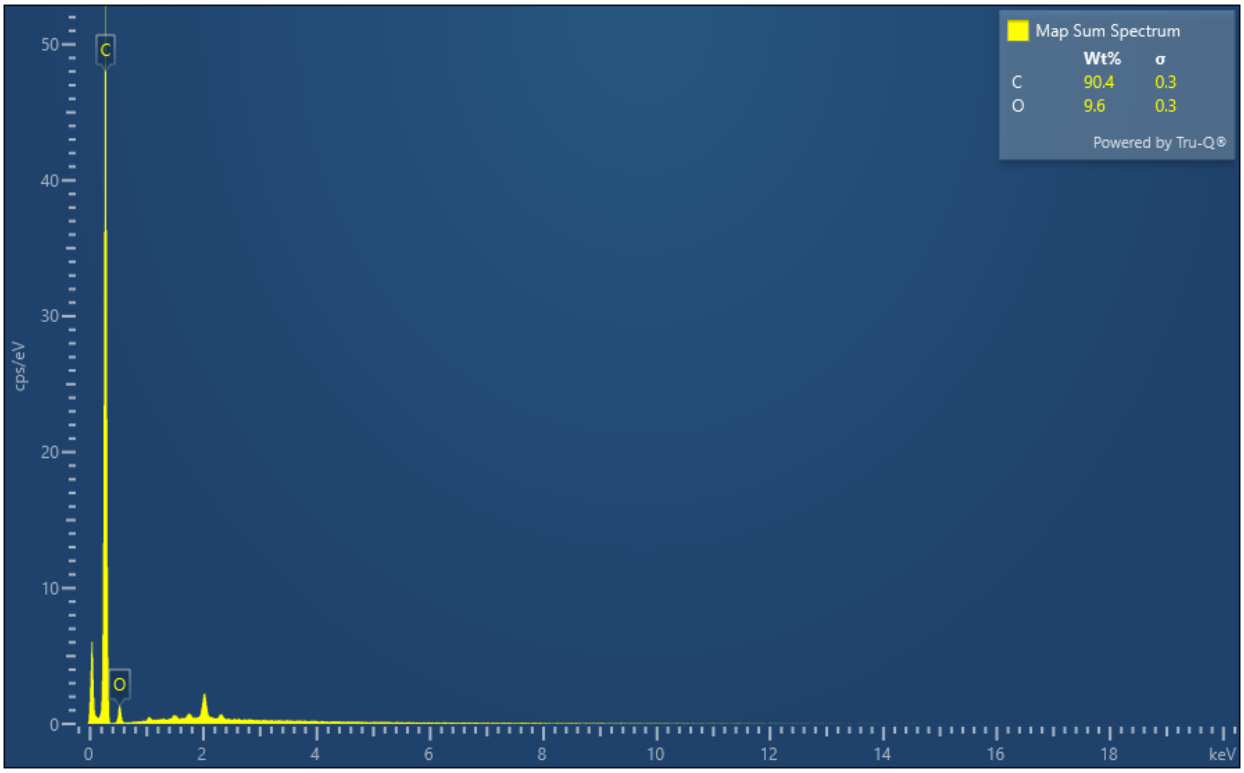
Map Sum Spectrum
Wt% σ
C 90.4 0.3
O 9.6 0.3
Powered by Tru-Q®
cps/eV
keV
C
O

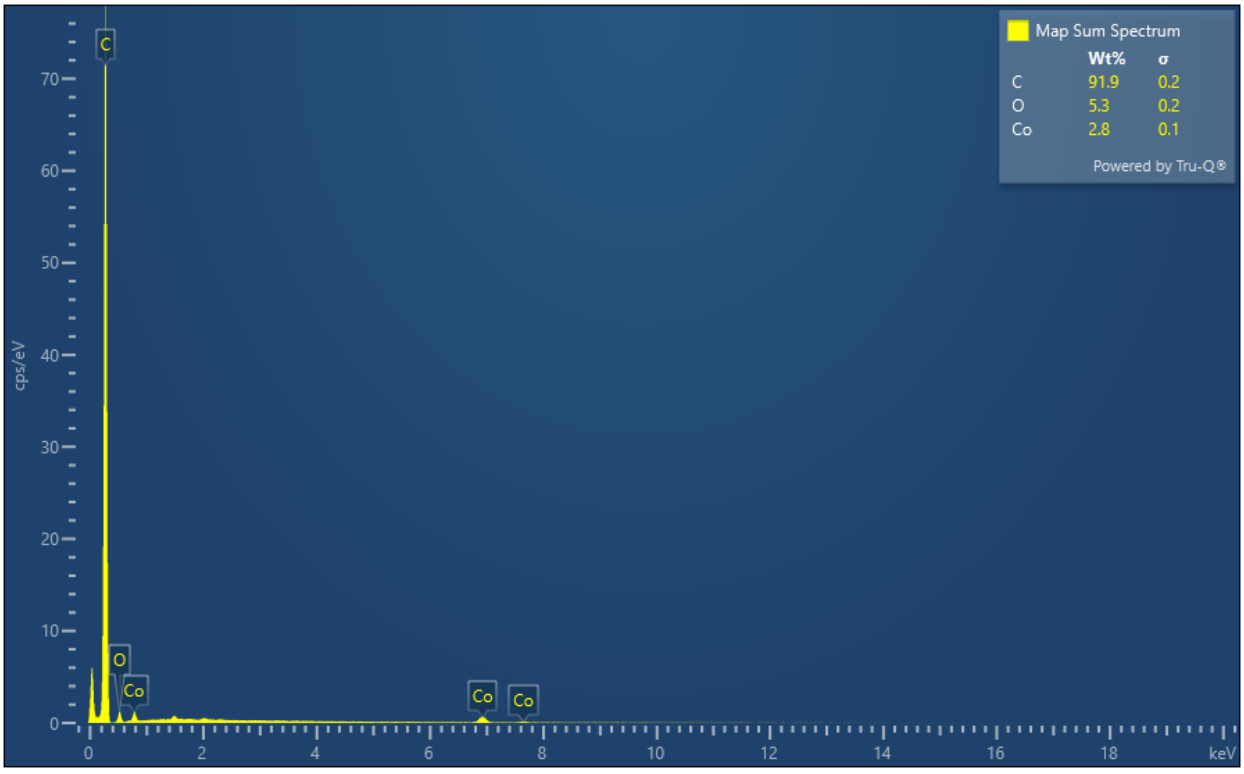
Map Sum Spectrum
Wt% σ
C 91.9 0.2
O 5.3 0.2
Co 2.8 0.1
Powered by Tru-Q®
cps/eV
keV
C
O
Co
Co
Co

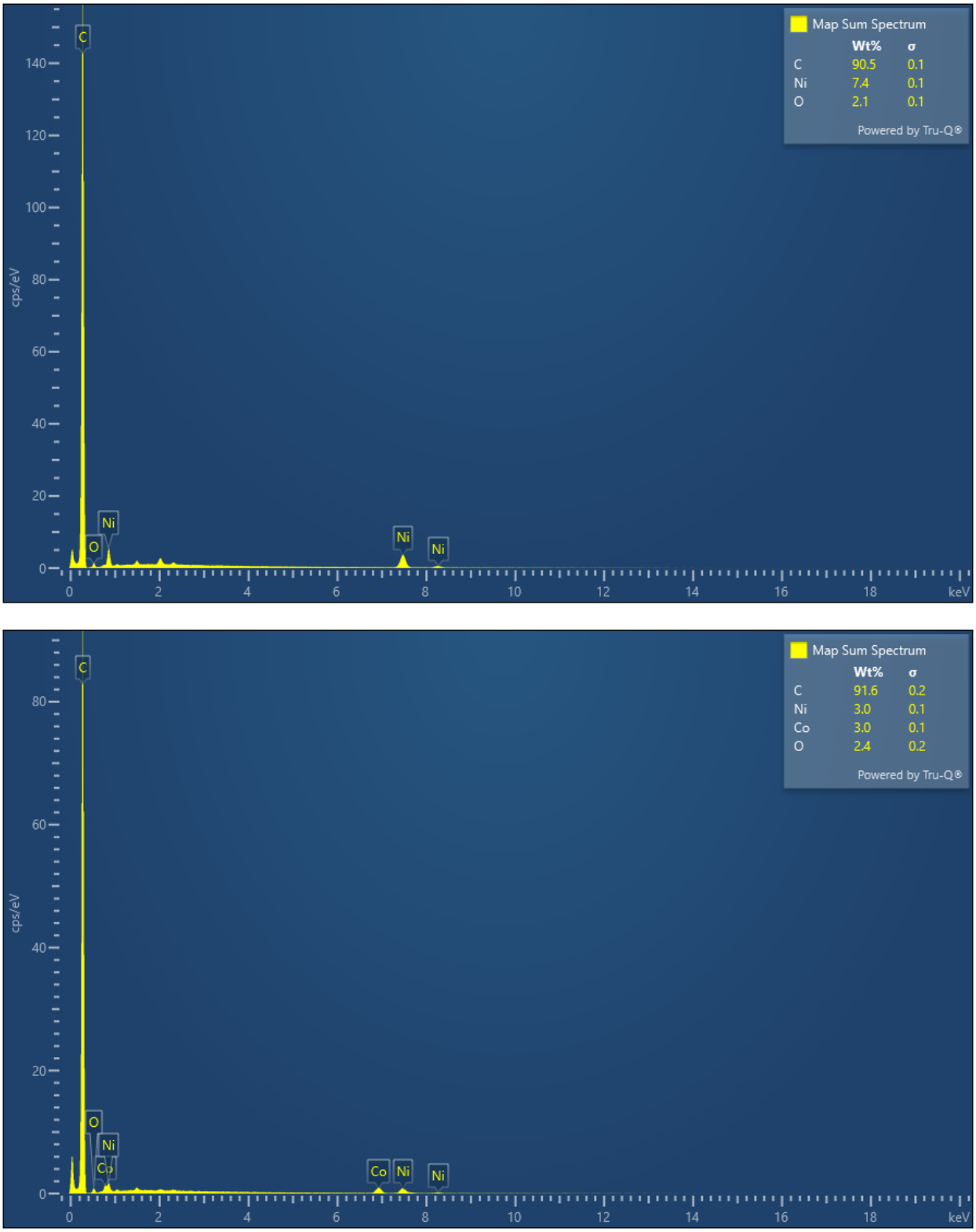

Appendix A- EDS spectra of RF-C, RF-CCo, RF-CNi, and RF-CCoNi

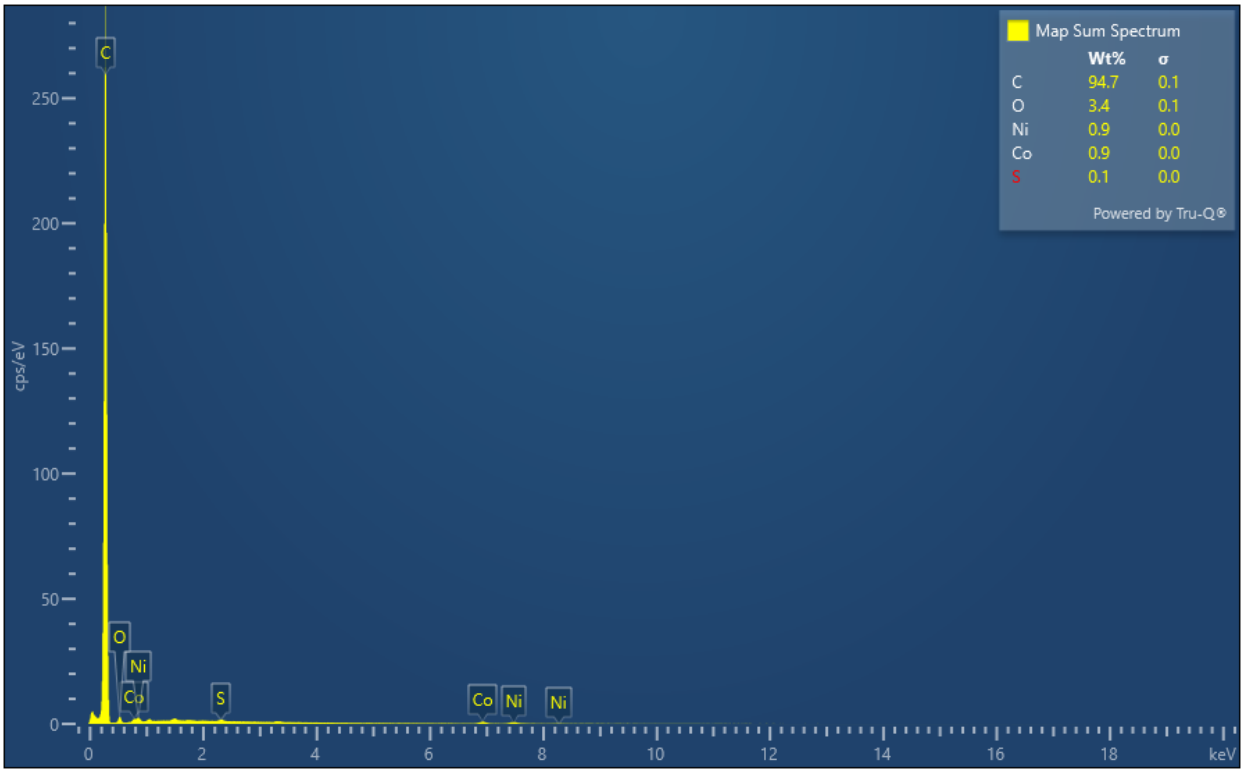
Map Sum Spectrum
Wt% σ
C 94.7 0.1
O 3.4 0.1
Ni 0.9 0.0
Co 0.9 0.0
S 0.1 0.0
Powered by Tru-Q®
cps/eV
keV
C
O
Ni
Co
S
Co
Ni
Ni

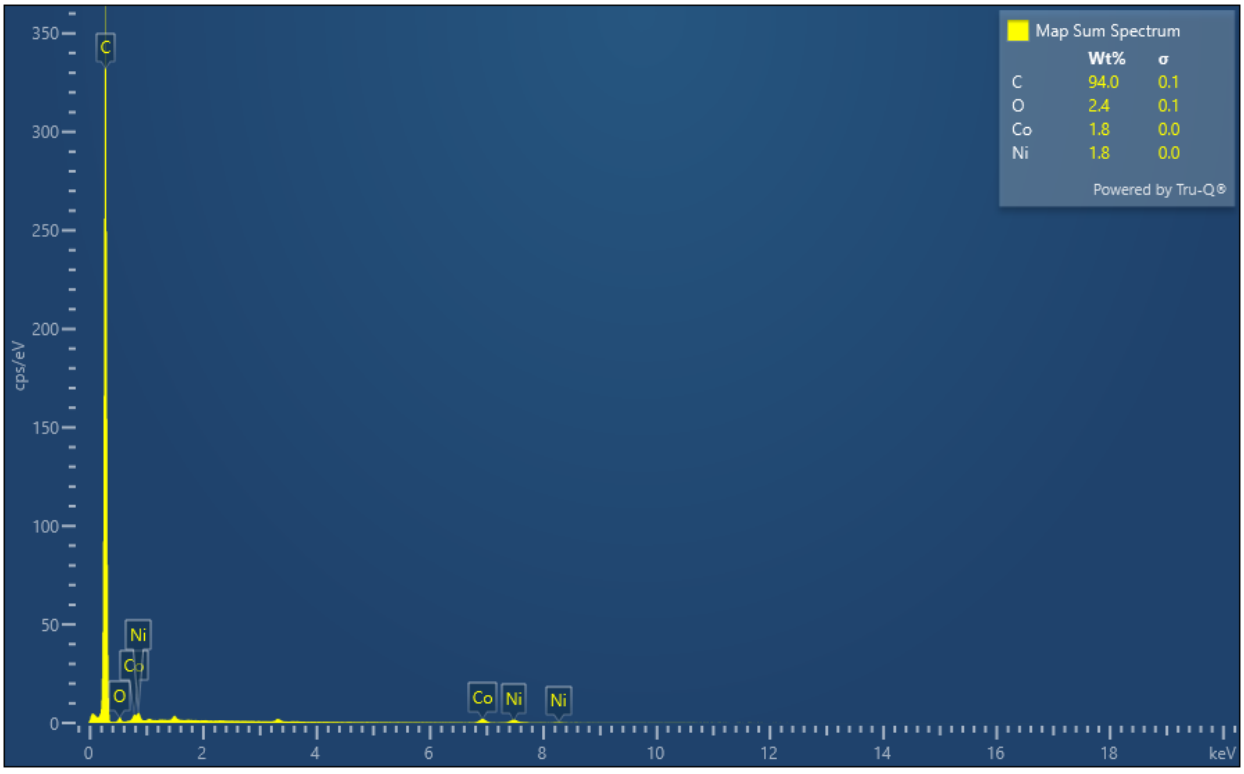
Map Sum Spectrum
Wt% σ
C 94.0 0.1
O 2.4 0.1
Co 1.8 0.0
Ni 1.8 0.0
Powered by Tru-Q®
cps/eV
keV
C
Ni
Co
O
Co
Ni
Ni

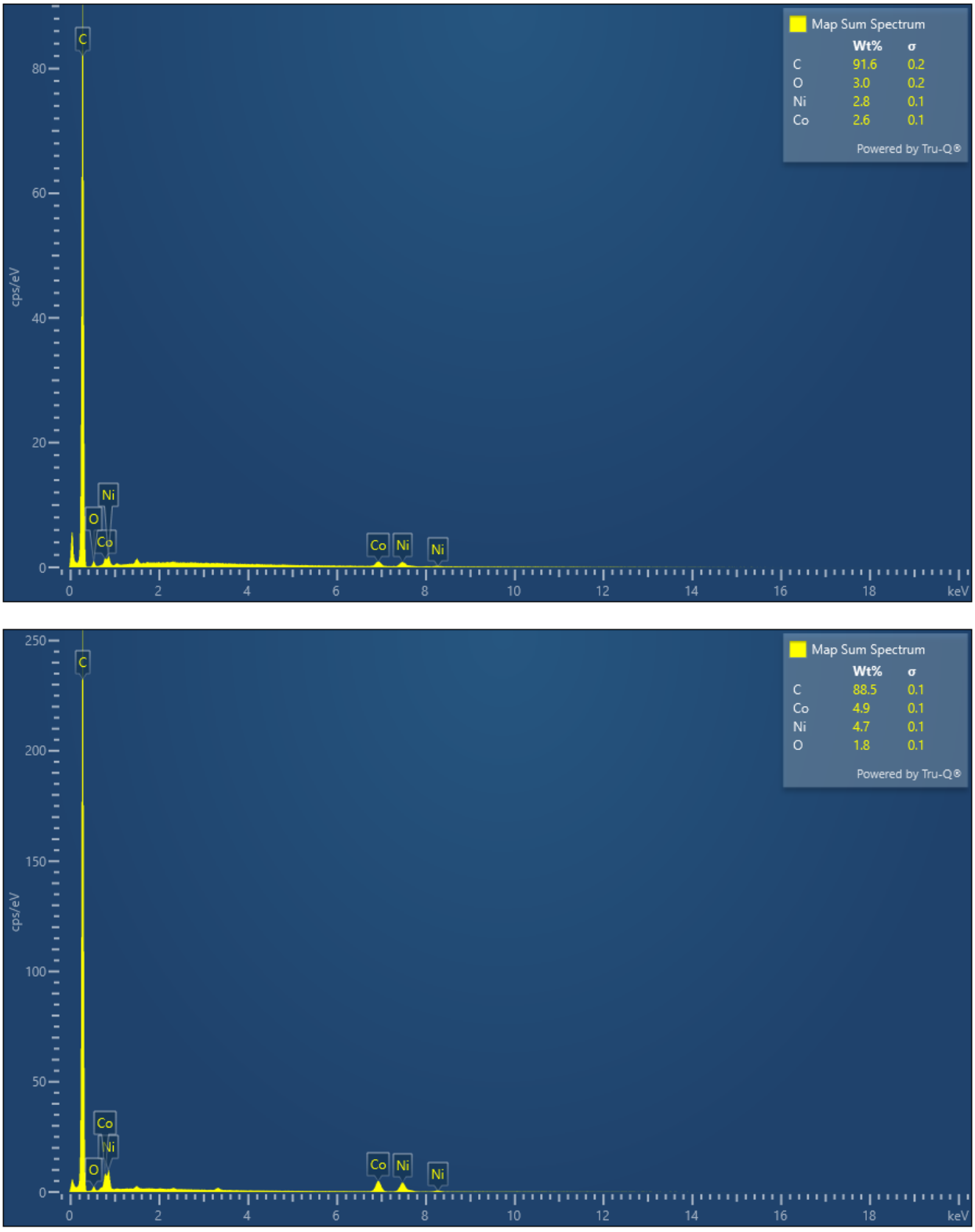

Appendix B- EDS spectra of RF-CCoNi 25%-150%

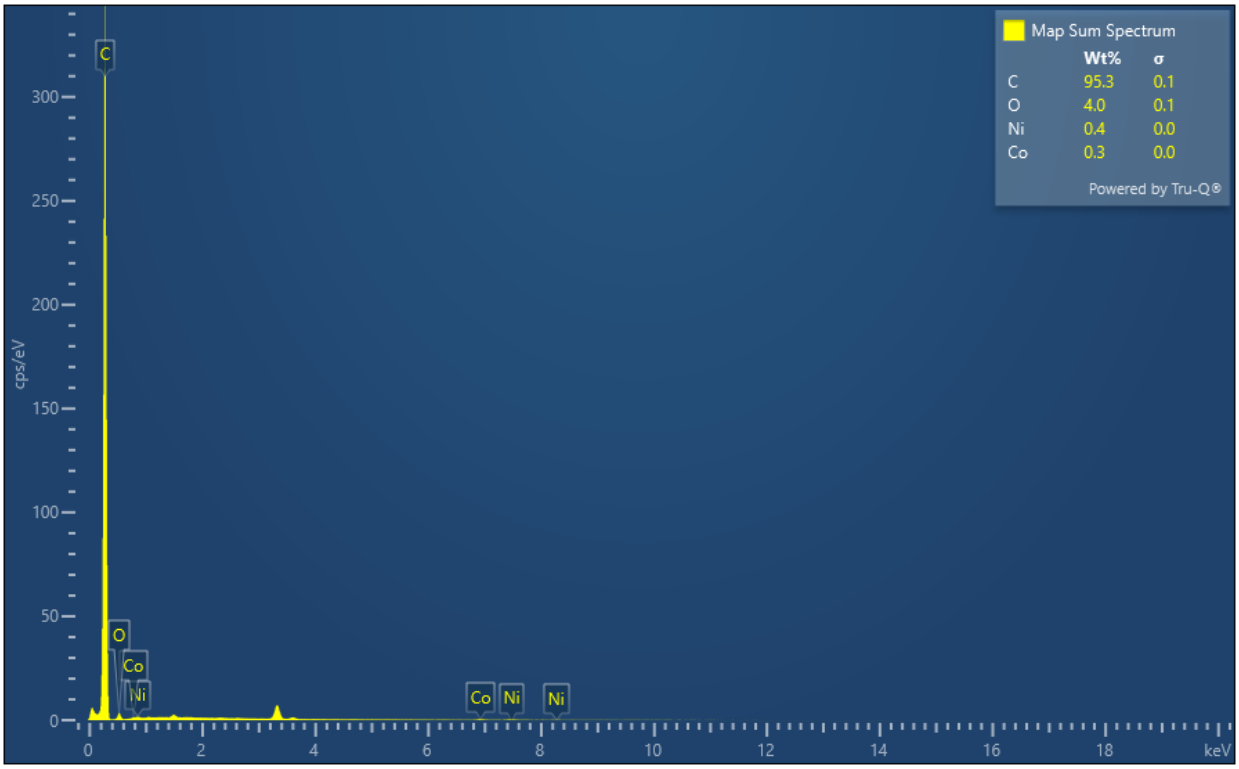
Map Sum Spectrum
Wt% σ
C 95.3 0.1
O 4.0 0.1
Ni 0.4 0.0
Co 0.3 0.0
Powered by Tru-Q®
cps/eV
keV
C
O
Co
Ni
Co
Ni
Ni

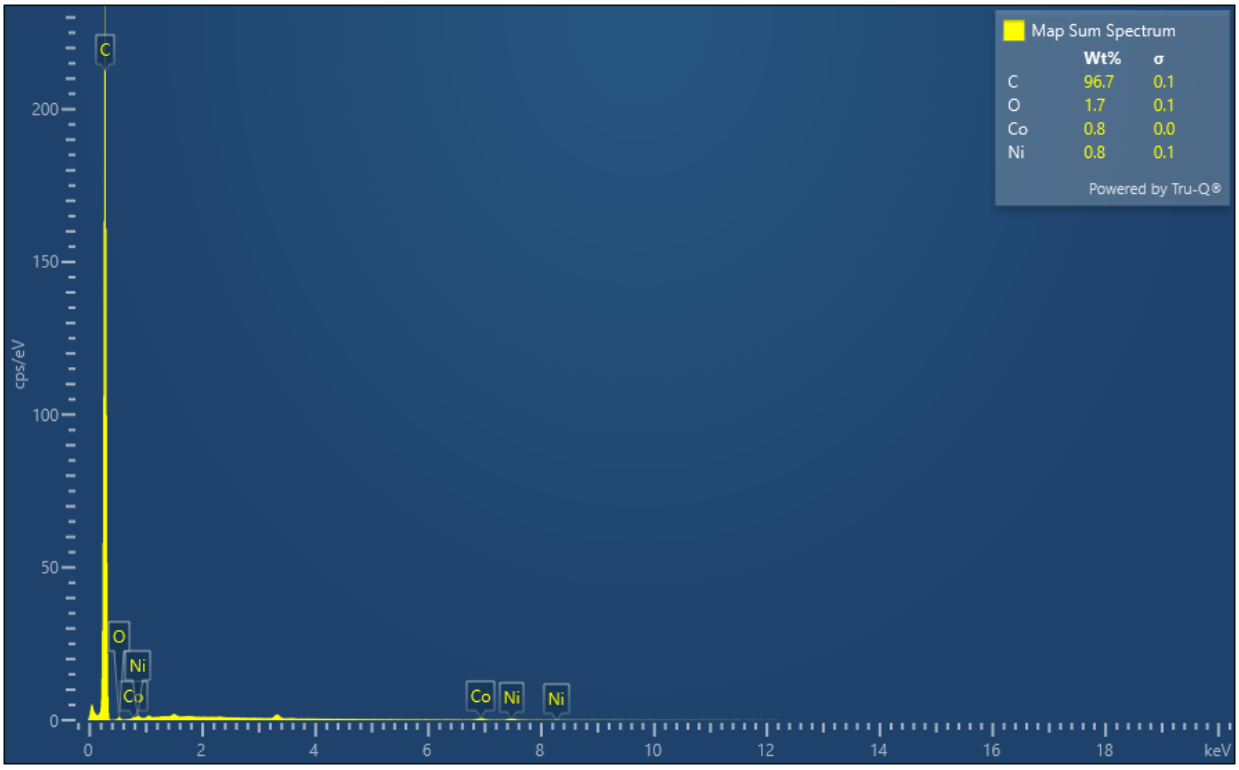
Map Sum Spectrum
Wt% σ
C 96.7 0.1
O 1.7 0.1
Co 0.8 0.0
Ni 0.8 0.1
Powered by Tru-Q®
cps/eV
keV
C
O
Ni
Co
Co
Ni
Ni

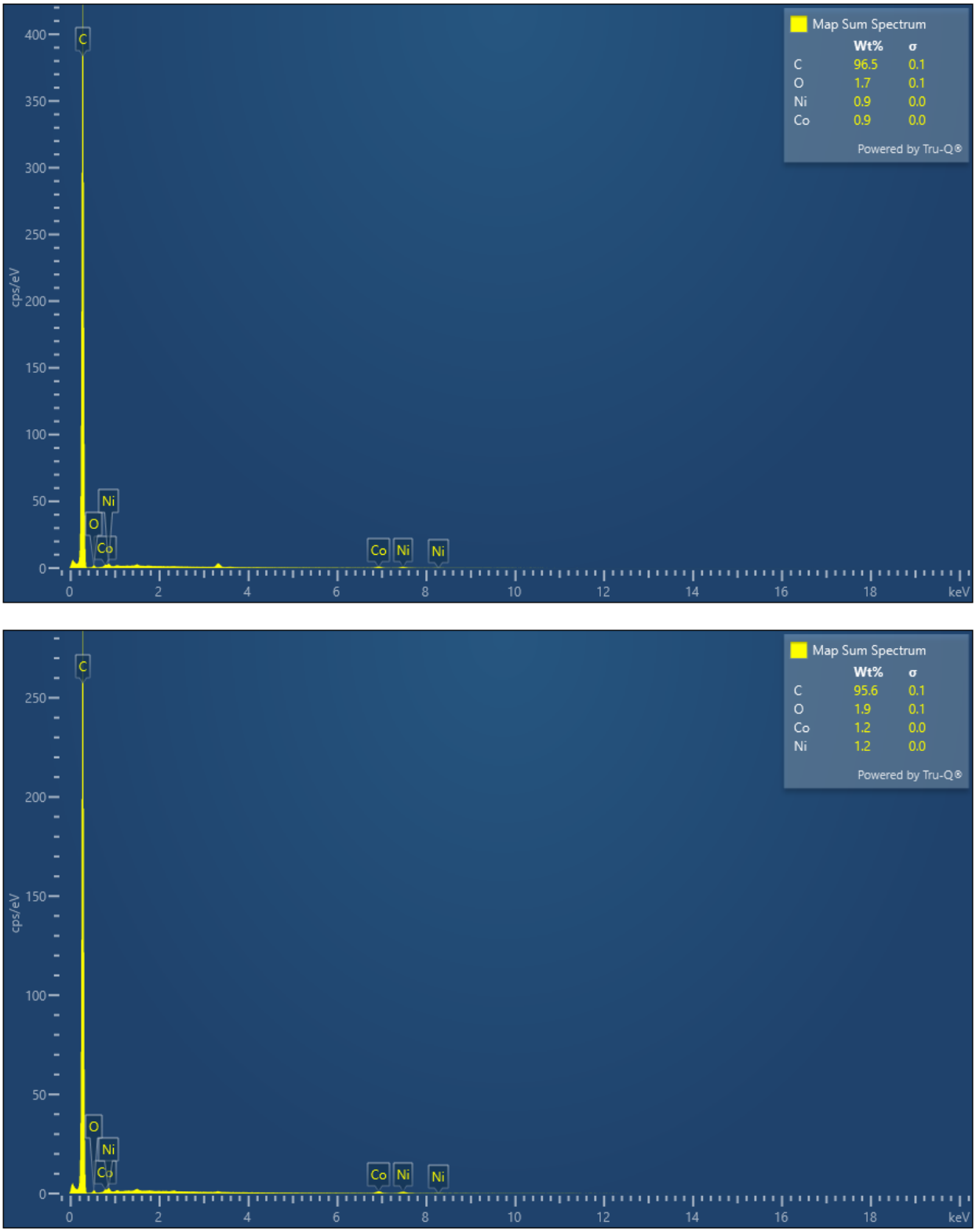

Appendix C- EDS spectra of RF-CCoNi 10%-40%